Institute for Advanced Technology
The University of Texas at Austin

IAT

Projectile-Flow Effect for Long Rod Penetration

Y. Partom
Institute for Advanced Technology
The University of Texas at Austin

December 1994

IAT.R 0036

DISCLAIMER NOTICE

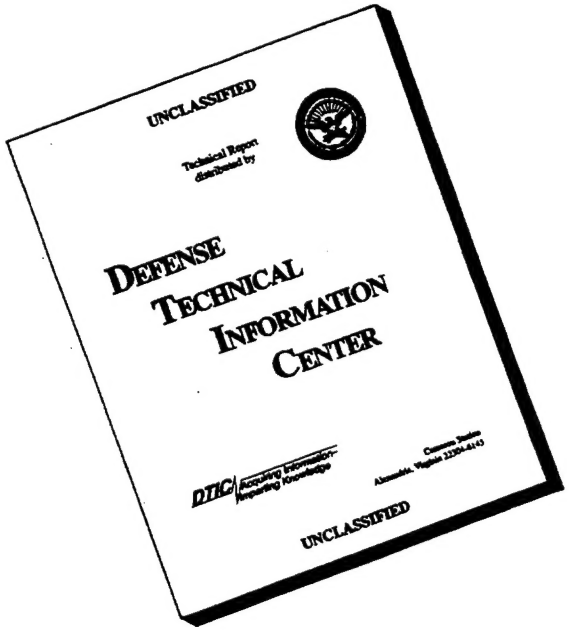

THIS DOCUMENT IS BEST QUALITY AVAILABLE. THE COPY FURNISHED TO DTIC CONTAINED A SIGNIFICANT NUMBER OF PAGES WHICH DO NOT REPRODUCE LEGIBLY.

REPORT DOCUMENTATION PAGE

Form Approved
OMB NO. 0704-0188

1. AGENCY USE ONLY (Leave blank)	2. REPORT DATE	3. REPORT TYPE AND DATES COVERED
	December 1994	Technical Report

4. TITLE AND SUBTITLE

Projectile-Flow Effect for Long Rod Penetration

5. FUNDING NUMBERS

Contract # DAAA21-93-C-0101

6. AUTHOR(S)

Y. Partom

7. PERFORMING ORGANIZATION NAME(S) AND ADDRESS(ES)

Institute for Advanced Technology
The University of Texas at Austin
4030-2 W. Braker Lane, #200
Austin, TX 78759

8. PERFORMING ORGANIZATION REPORT NUMBER

IAT.R 0036

9. SPONSORING / MONITORING AGENCY NAME(S) AND ADDRESS(ES)

U.S. Army Research Laboratory
ATTN: AMSRL-WT-T
Aberdeen Proving Ground, MD 21005-5066

10. SPONSORING / MONITORING AGENCY REPORT NUMBER

11. SUPPLEMENTARY NOTES

The view, opinions and/or findings contained in this report are those of the author(s) and should not be considered as an official Department of the Army position, policy, or decision, unless so designated by other documentation.

12a. DISTRIBUTION / AVAILABILITY STATEMENT

Approved for public release; distribution unlimited.

12b. DISTRIBUTION CODE

A

13. ABSTRACT *(Maximum 200 words)*

There have been indications that the flow stress level in the plastically flowing part of a long rod penetrator may have a significant influence on the penetration efficiency.

We refer to this phenomenon as the projectile-flow effect. We performed a series of AUTODYN runs to investigate the projectile-flow effect. We show that when the projectile material hardens/softens as it flows, its penetration can be reduced/enhanced significantly.

We also show that the projectile-flow effect is less pronounced at high velocities, and is enhanced for high L/D penetrators. It seems that the L/D effect at high L/D may be explained by the projectile-flow effect.

14. SUBJECT TERMS

flow stress, hypervelocity, L/D effects, long rod penetrator, penetration efficiency

15. NUMBER OF PAGES

88

16. PRICE CODE

17. SECURITY CLASSIFICATION OF REPORT	18. SECURITY CLASSIFICATION OF THIS PAGE	19. SECURITY CLASSIFICATION OF ABSTRACT	20. LIMITATION OF ABSTRACT
Unclassified	Unclassified	Unclassified	UL

Table of Contents

List of Tables

List of Figures

List of Figures

Projectile-Flow Effect for Long Rod Penetration

Yehuda Partom

Abstract

There have been indications that the flow stress level in the plastically flowing part of a long rod penetrator may have a significant influence on the penetration efficiency.

We refer to this phenomenon as the "projectile-flow effect." We performed a series of AUTODYN runs to investigate the projectile-flow effect. We show that when the projectile material hardens/softens as it flows, its penetration can be reduced/enhanced significantly.

We also show that the projectile-flow effect is less pronounced at high velocities, and is enhanced for high L/D penetrators. It seems that the L/D effect at high L/D may be explained by the projectile-flow effect.

1. Introduction

Magness [1], investigating why DU long rod projectiles outperform tungsten alloy projectiles at ordnance velocities, proposed the following concept:

> "...adiabatic shear behavior of uranium aids its performance by minimizing the size of the mushroom head on the eroding penetrator. The uranium projectile would therefore penetrate more efficiently, making a smaller diameter penetration tunnel, but achieving greater penetration depth."

Bruchey, et al., [2] performed tests with single crystal tungsten L/D=15 projectiles at three different crystal orientations. They discovered that the three orientations had different penetration efficiencies and concluded that:

> "Favorable slip/cleavage during the compressive loading of the penetration process to allow penetrator material flow without large scale plastic deformation, and, final shear localization at a favorable angle for easy

material flow away from the penetration interface, contribute to t [00] orientation crystals excellent performance. The net result was less ergy expenditure during penetrator flow and, therefore, more energy fo efor- mation of RHA."

Partom and Yaziv [3], investigating the L/D effect for large L/D performed simulations with the PISCES2D wavecode in which they introduced finite strain to failure (ε_f) for the projectile. They obtained that: "Penetration iency increases with decreasing values of ε_f for both L/D=10 and L/D=20 projectiles," and that "the increase in penetration efficiency when ε_f is reduced is much larger for L/D=20 projectiles than for L/D=10 projectiles."

Reaugh [4] performed simulations with the GLO wavecode in which DU and tungsten alloy L/D=10 and 20 rods penetrated RHA targets. He introduced strain hardening and thermal softening for the projectile material and showed that "...projectile material properties that foster the residue hugging the crater wall (thermal softening in our simulations and adiabatic shear fracture in the experiments) result in higher penetration depth."

The results obtained in these studies indicate that the penetration efficiency of long rods may be significantly dependent on the flow stress of the radially flowing projectile, and not just on its yield strength. When the projectile material is hardening or softening as it flows, the dependence of the penetration efficiency on the hardening/softening seems to be counterintuitive. A hardening material would penetrate less and a softening material may penetrate more. The results also indicate that the mechanisms by which the hardening or softening is achieved are not important. It is the end result, the flow stress of the flowing material, that affects the penetration efficiency. We refer to this behavior of long rod penetrators as the "Projectile-Flow Effect."

In what follows, we investigate systematically the projectile flow effect by means of computer simulations using the AUTODYN wavecode. We performed four sets of simulations:

Set No. 1.

In which the projectile material is linearly hardening (softening) by:

$$Y = Y_o \left(1 + \beta\, \varepsilon^p_{eff}\right) \ , \qquad (1)$$

where ε^p_{eff} is the effective plastic strain, β is positive/negative for hardening/softening, respectively, the impact velocity is V = 1.5 km/s and L/D=10.

Set No. 2.

Which is the same as Set No. 1, except that V = 2.5 km/s, to see how the projectile flow effect changes with velocity.

Set No. 3.

Which is the same as Set No. 1, except that L/D=20, to see how the projectile flow effect changes with L/D.

Set No. 4.

In which the projectile material has a constant flow stress up to a given value of the effective plastic strain ($\varepsilon^p_{eff} = \varepsilon_j$), and then changes to another value:

$$Y = Y_o \text{ for } 0 < \varepsilon^p_{eff} < \varepsilon_j \,, \qquad (2)$$

$$Y = Y_j \text{ for } \varepsilon_j < \varepsilon^p_{eff} \,.$$

Among other combinations, we used:

$$Y_j = 0 \,, \qquad (3)$$

for which ε_j is equivalent to a strain to failure (ε_f), and

$$Y_j = 2Y_o \,. \qquad (4)$$

The purpose of this Set (in conjunction with Set No. 1) is to show that the projectile-flow effect does not depend on a specific hardening/softening law.

As a special case, we used $\varepsilon_j = \infty$ (which is equivalent to $Y = Y_o$ = const.), with different values of Y_o. The purpose of these runs is to show that the projectile-flow effect is always active, even for the constant flow stress case.

2. Simulations

We are using the Euler processor of AUTODYN version 2.65, on a DELL 486 PC 466M with 32MB RAM. This allows for a maximum grid of 60,000 cells.

The tungsten alloy (projectile) and RHA steel (target) material models and parameters are the same as in reference [5]. We use a Mie-Gruniesen equation of state (EOS) referenced to the shock adiabat with the parameters listed in Table 1.

Table 1
EOS Parameters

	Steel	Tungsten Alloy
ρ_o (g/cc)	7.85	17.3
C_o (km/s)	3.57	4.03
S	1.92	1.26
Γ_o	1.7	1.7
P_{min} (GPa)	-2.	-2.

where ρ = density, C_o, S are the shock velocity particle velocity Hugoniot parameters, Γ_o = Gruneisen parameter, and P_{min} is the spall strength.

For the stress deviator we use a constant shear modulus G and a von-Mises yield surface with a yield strength Y_o as shown in Table 2.

Table 2
Shear Stress Parameters

	Steel	Tungsten Alloy
G (GPa)	80	140
Y_o (GPa)	1	2

The flow stress Y is determined by the hardening/softening law as outlined in the Introduction.

In all runs the projectile radius is D/2 = 5 mm, and the Euler cell size is 1 x 1 mm so that there are five cells across the radius. This may not be enough to obtain convergent results (as many as seven or eight cells across the radius are needed). But as our purpose is to compare among simulation results (and not between simulations and experiments), five cells across the radius would seem satisfactory. Target dimensions varied from one set of runs to another as shown in Table 3.

Table 3
Target Dimensions

Set No.	L/D	V (km/s)	Radius $D_t/2$ (mm)	Thickness L_t (mm)
1	10	1.5	100	150
2	10	2.5	150	200
3	20	1.5	100	250
4	10	1.5	100	150

3. Set No. 1: Linear Hardening/Softening

As mentioned in the Introduction, linear hardening/softening is specified by:

$$Y = Y_o \left(1 + \beta\, \varepsilon_{eff}^{p}\right) \ , \tag{5}$$

where Y_o is the initial yield stress, Y is the (subsequent) flow stress, ε_{eff}^{p} is the effective plastic strain, and β is the hardening ($\beta > 0$)/softening ($\beta < 0$) parameter. There are seven runs in which β varies in the range $-0.25 \le \beta \le 1.00$. The penetration efficiencies (P/L, where P = Penetration) obtained in these runs are listed in Table 4, and plotted in Figure 1.

Table 4
Penetration Efficiency (P/L) for Set No. 1 Runs

β	P/L
-0.25	0.92
-0.10	0.85
0.00	0.81
+0.10	0.75
+0.25	0.67
+0.50	0.51
+1.00	0.42

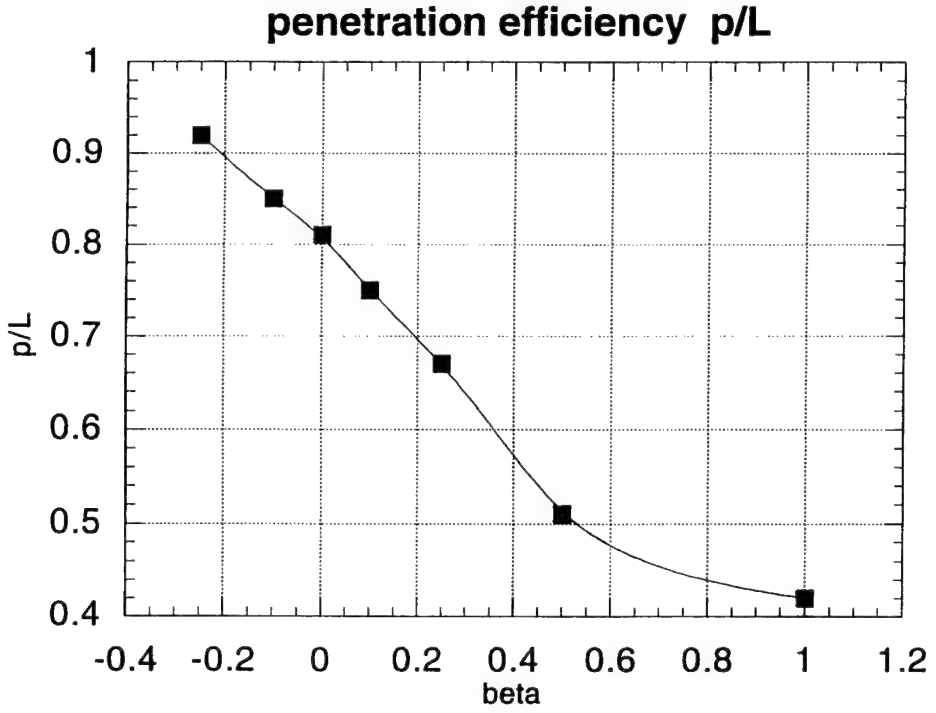

Figure 1. Penetration efficiency as function of the hardening/softening parameter for Set No. 1.

We see that for $\beta < 0.5$, P/L decreases approximately linearly with β. For higher values of β the decrease tends to saturate. This shows that a softening projectile material can have a substantially higher efficiency than a hardening material with the same initial yield strength.

In Figure 2, we show the penetration-erosion (PL) curves obtained in the seven runs of Set No. 1. We see that for $\beta > 0$ (hardening), there is practically no quasi-steady-state regime. Also, the secondary penetration regime becomes less pronounced as β increases.

In Figure 3, we show penetration velocity histories for four of the seven runs. We see clearly that the degree of deceleration increases with β. But the different curves start to deviate from each other only after about 20 μs, or after a penetration of about 15 mm. It seems that the initial deceleration is not sensitive to the degree of hardening/softening.

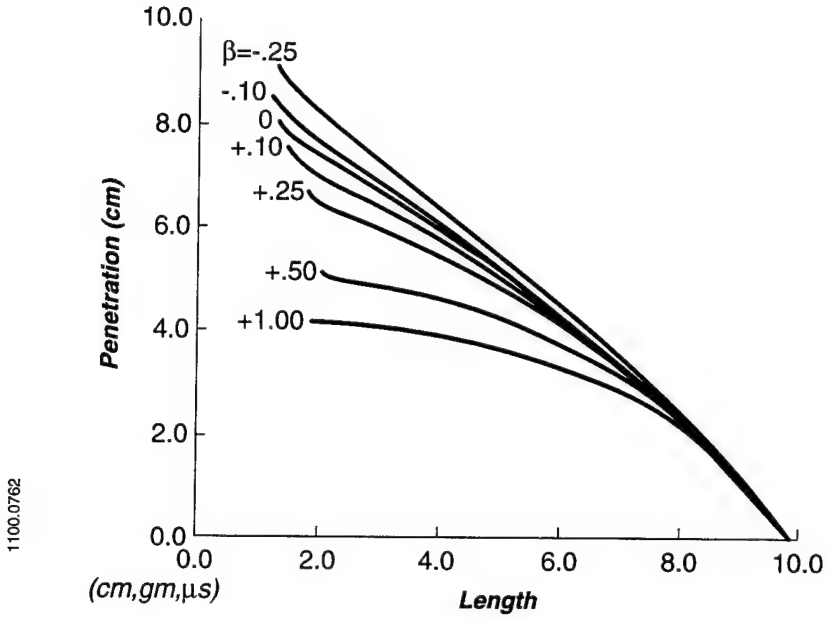

Figure 2. Penetration-erosion curves for Set No. 1.

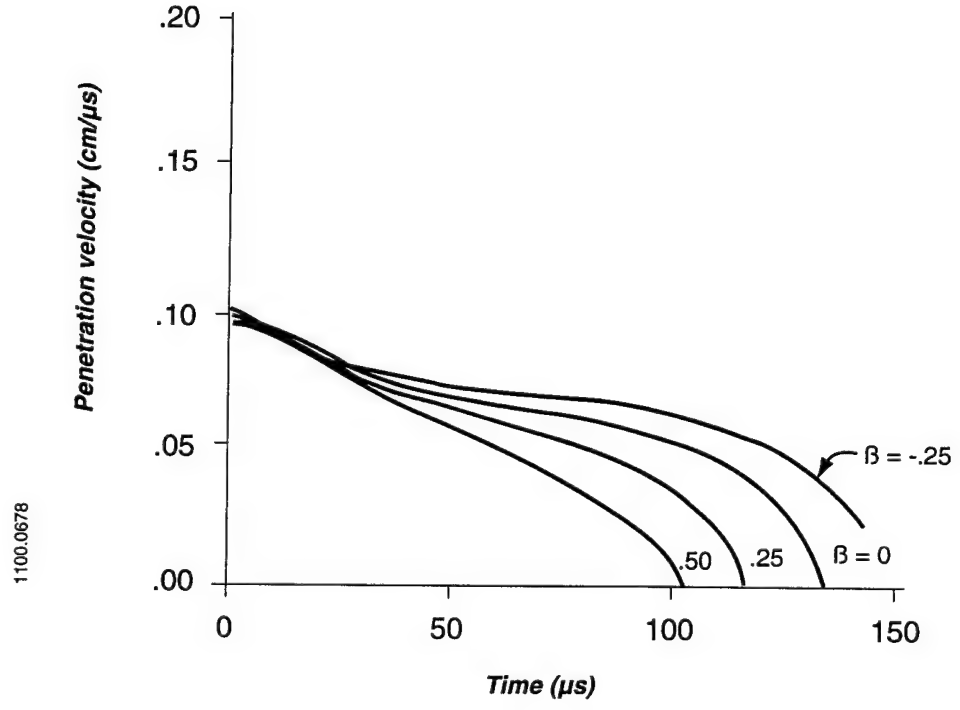

Figure 3. Penetration velocity histories for Set No. 1.

In Figure 4, we show the final crater and projectile configurations for the seven runs. For $\beta \leq 0$, the configurations look similar; however, as β increases, the residual projectile length (L_f) is larger, the inverted projectile tube length is shorter and the crater diameter is somewhat larger. For a high hardening rate ($\beta > 0.25$) there is no tube, the crater widens towards its bottom, and the residual projectile has a spherical shape.

In Appendix A we give, for documentation purposes, detailed plots for each of the runs. These include: history plots, material status, velocity vectors, and effective plastic strain contour plots (except for $\beta = 0$) every 400 cycles.

4. Set No. 2: Effect of Impact Velocity (V = 2.5 km/s)

We expect that at a high impact velocity the projectile flow effect would be less pronounced. A plausible argument is that at a high impact velocity, strength effects in general are less important compared to inertia effects. The purpose of Set No. 2 runs is therefore to validate our expectation about the projectile flow effect at high velocities, and to quantify the effect as a function of impact velocity.

We made three runs, at β = -0.25, 0, and 0.25. The penetration efficiencies obtained are listed in Table 5.

Table 5
Penetration Efficiencies for Set No. 2

β	P/L
-0.25	1.44
0.00	1.41
0.25	1.37

We see that, as expected, they vary much less than for 1.5 km/s (Table 4). To see this more clearly, we show in Figure 5 the penetration efficiency as a function of β for both V = 1.5 and 2.5 km/s. The average slope $d(P/L)/d\beta$ in the range $-0.25 \leq \beta \leq 0.25$ as obtained from the figure is -0.49 for 1.5 km/s and -0.15 for 2.5 km/s. In Figures 6, 7, 8, and 9, we show history curves from the runs of Set No. 2.

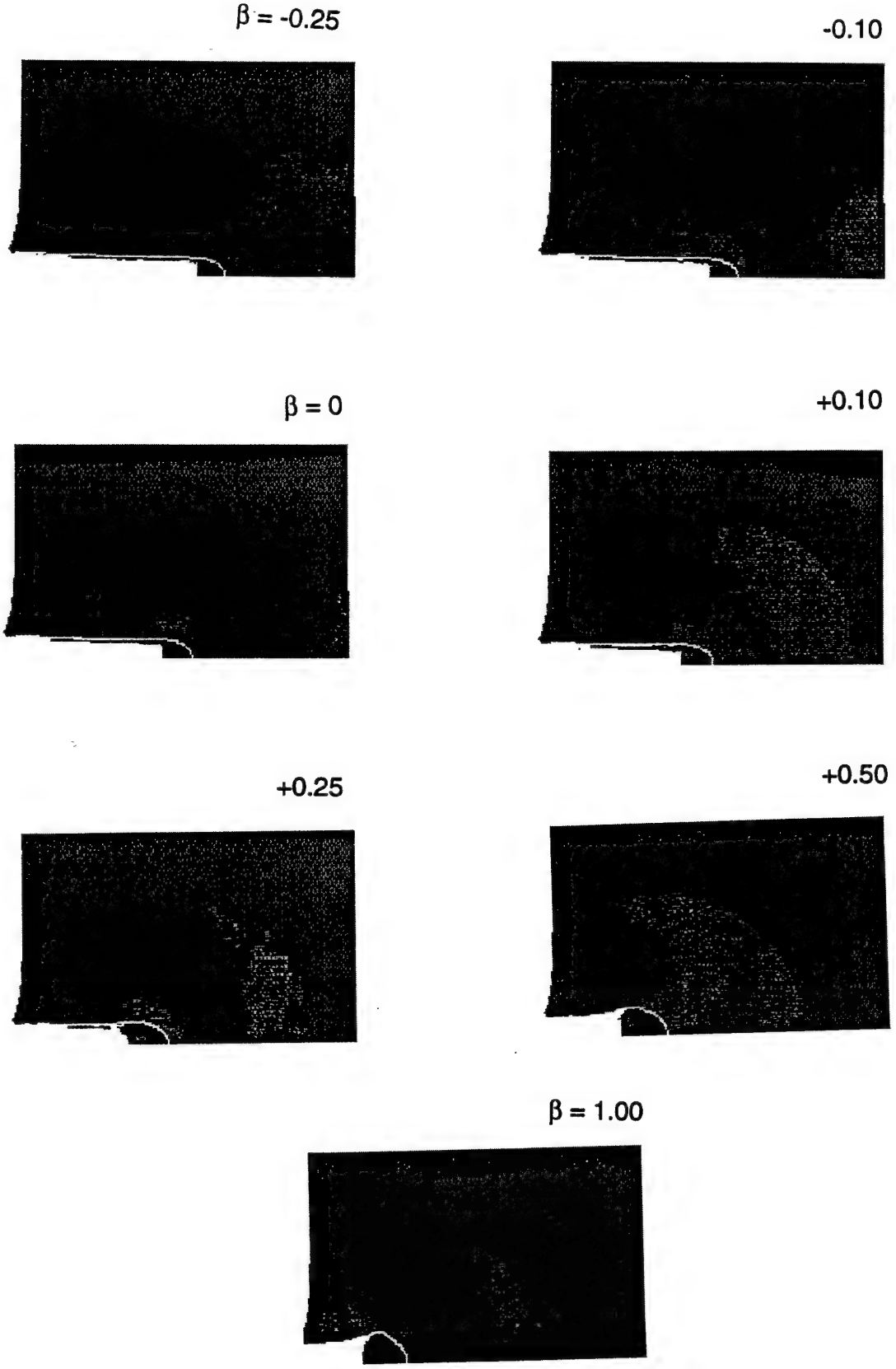

Figure 4. Final crater and projectile configuration for runs of Set No. 1.

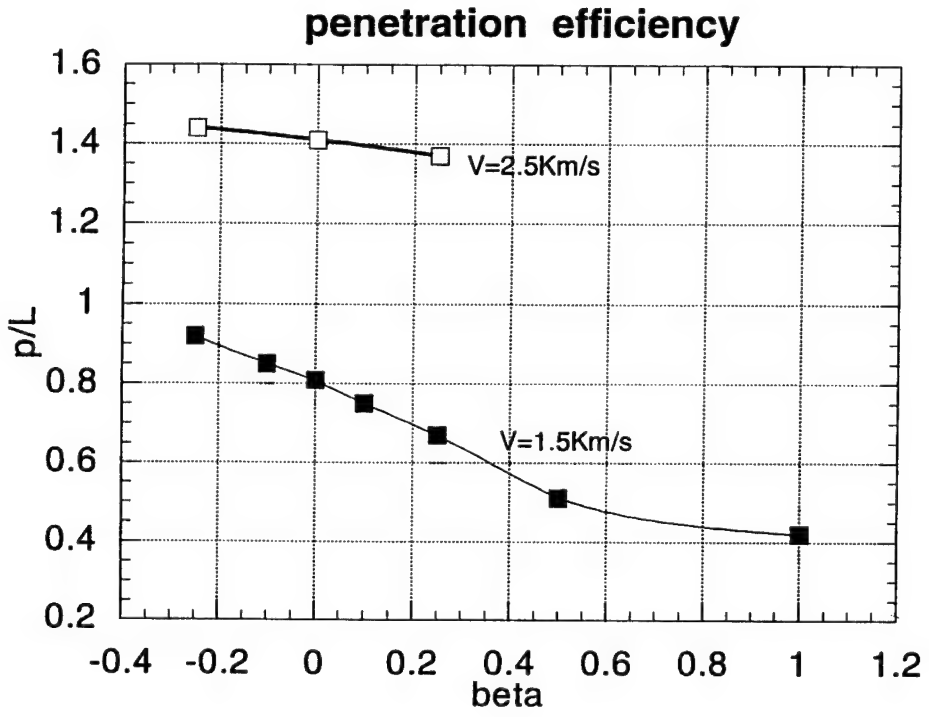

Figure 5. Penetration efficiency (P/L) as function of hardening parameter (β) for Set No. 1 (V = 1.5 km/s) and Set No. 2 (V = 2.5 km/s).

In Figure 6, we show penetration-erosion curves. In Figure 7, we show penetration histories. In Figures 8.1, 8.2, and 8.3, we show interface velocity and projectile tail velocity as a function of penetration. In Figure 9, we show the tail velocity as a function of penetration.

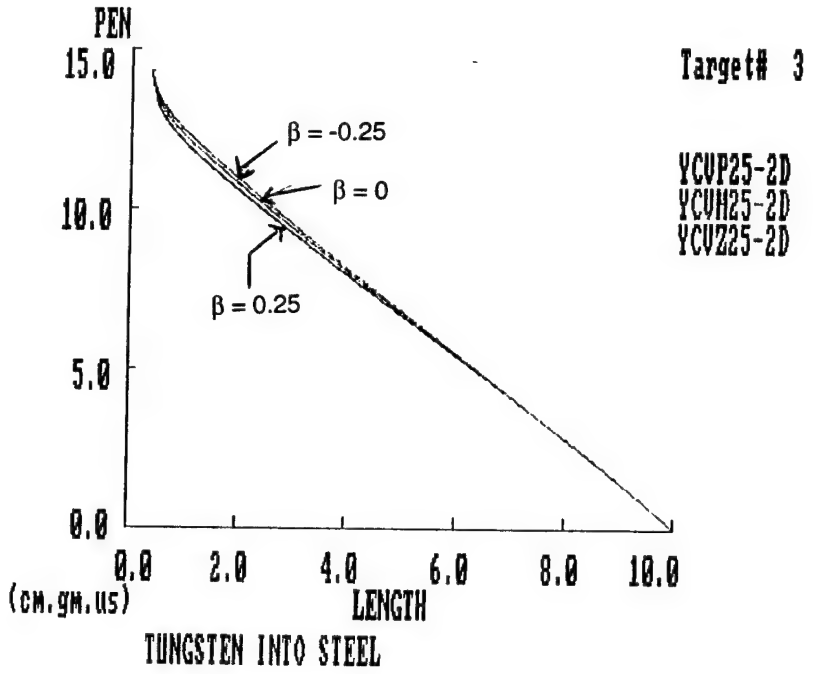

Figure 6. Penetration erosion curves for Set No. 2.

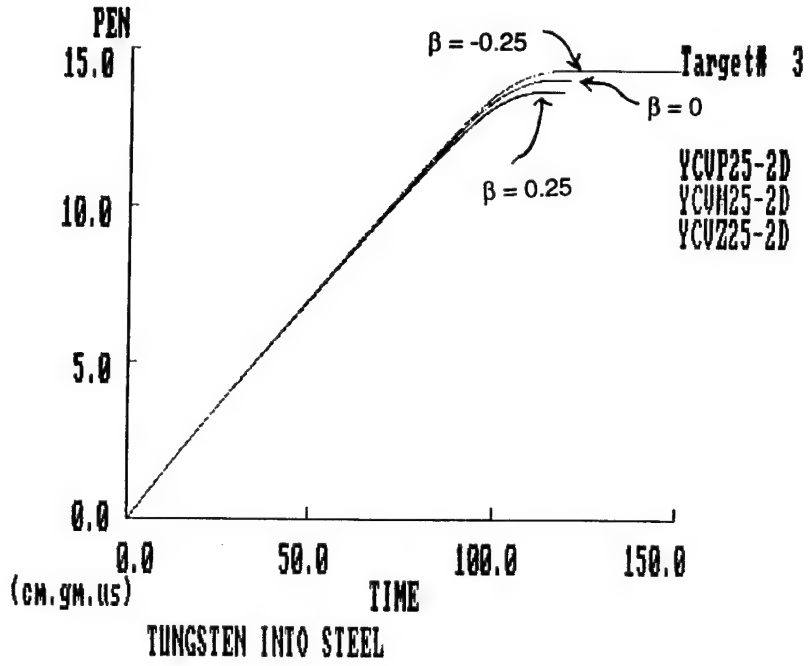

Figure 7. Penetration histories for Set No. 2.

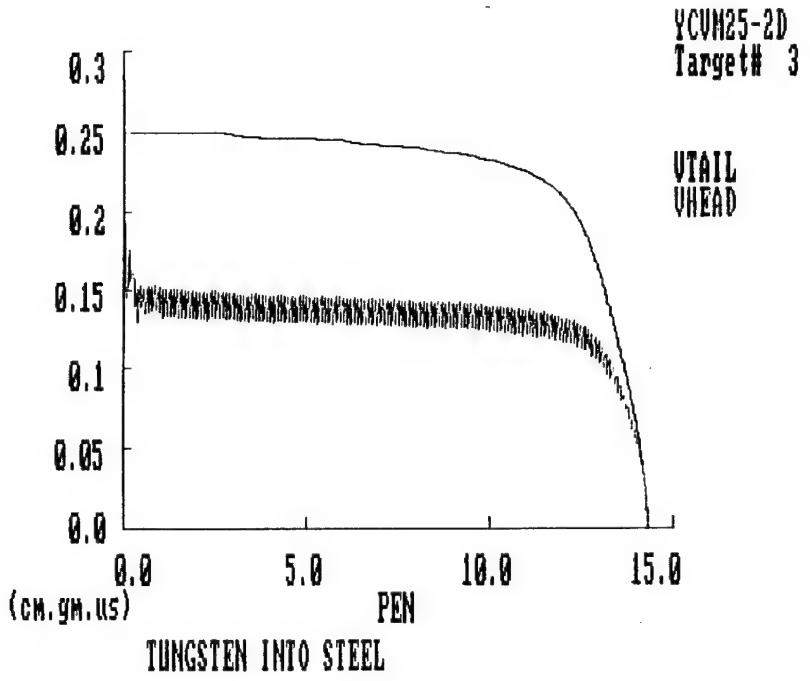

Figure 8.1. Interface velocity (VHEAD) and tail velocity (VTAIL) as a function of penetration (PEN) for β = -0.25 (Set No. 2).

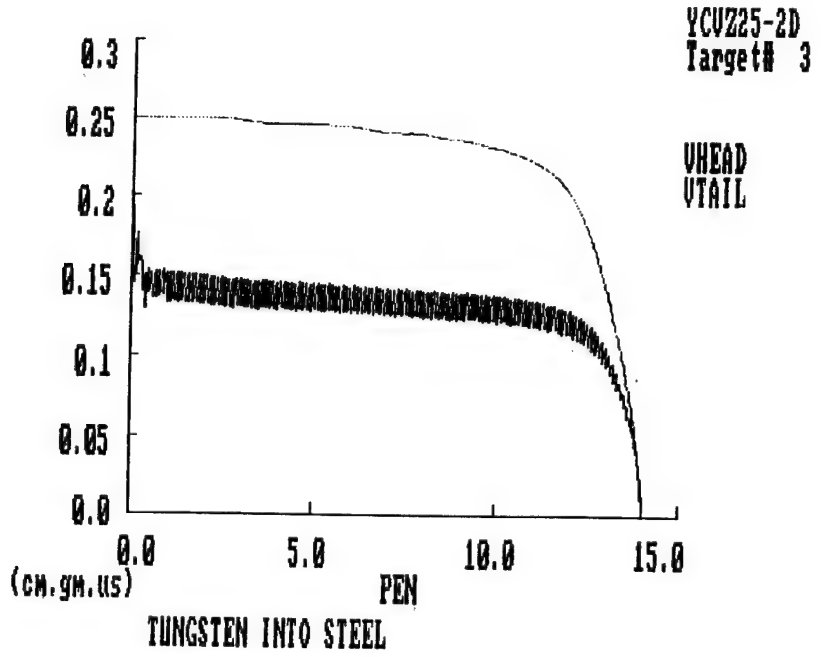

Figure 8.2. Interface velocity (VHEAD) and tail velocity (VTAIL) as a function of penetration (PEN) for β = 0 (Set No. 2).

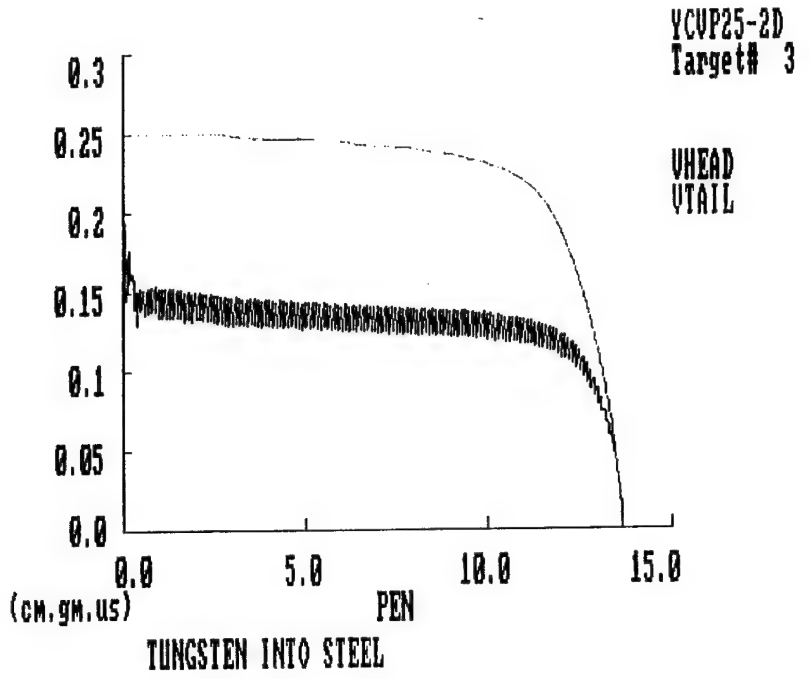

Figure 8.3. Interface velocity (VHEAD) and tail velocity (VTAIL) as a function of penetration (PEN) for $\beta = 0.25$ (Set No. 2).

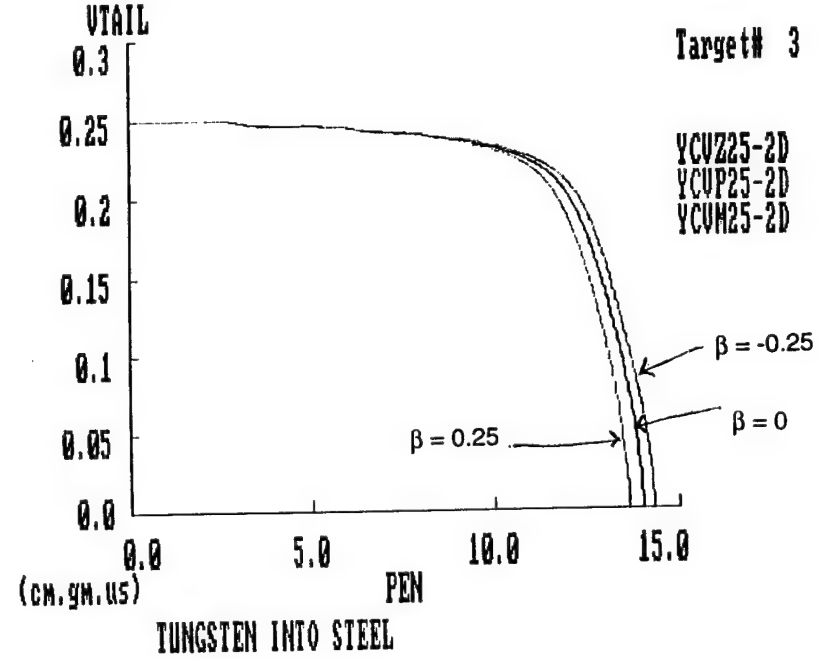

Figure 9. Tail velocity (VTAIL) as a function of penetration (PEN) for Set No. 2.

5. Set No. 3: Effect of L/D

We expect that for higher L/D the projectile flow effect wo' l be more pronounced. This is based on previous computations done with the wa' ode PISCES 2D [3]. The purpose of Set No. 3 is therefore to validate our expectat' is about the projectile-flow effect for high L/D projectiles, and to quantify the effec' a function of L/D.

We made three runs, at β = -0.25, 0, and 0.25. The penetration efficiencies obtained are listed in Table 6.

Table 6
Penetration Efficiencies for Set No. 3

β	P/L
-0.25	0.803
0.00	0.652
0.25	0.394

We see that the variation is much higher than for L/D=10 (Table 4). To see this more clearly, we show in Figure 10 the penetration efficiency as a function of β for both L/D=10 and 20 (at 1.5 km/s). The average slope $d(P/L)/d\beta$ in the range $-0.25 \leq \beta \leq .25$, as obtained from the figure, is -0.69 for L/D=10 and -0.60 to -1.0 for L/D=20.

In Figure 11, we show the final configuration of the penetration process for the three runs. It is evident that the hardening/softening parameter has a large influence. At β = 0.25, we already get a sphere-like residual projectile; for L/D=10 this happens only at β = 0.50. In Figures 12, 13, 14, and 15, we show history curves from the runs of Set No. 3.

In Figure 12, we show penetration-erosion curves. In Figure 13, we show penetration histories. In Figures 14.1, 14.2, and 14.3, we show interface velocity and projectile tail velocity as a function of penetration. In Figure 15, we show tail velocities as a function of penetration.

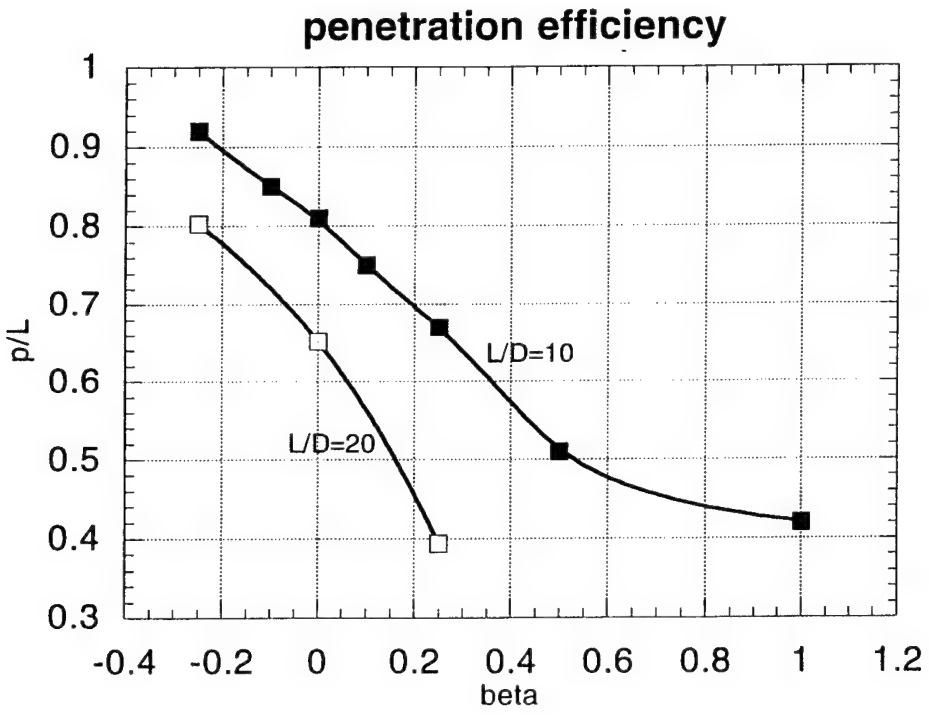

Figure 10. Penetration efficiency (P/L) as a function of hardening parameter (β) for Set No. 1 (L/D=10) and Set No. 3 (L/D=20).

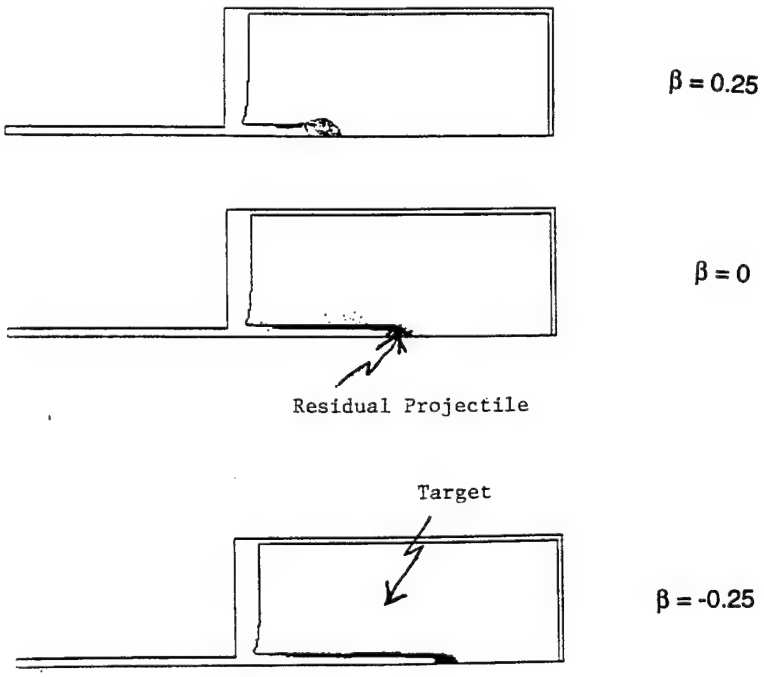

Figure 11. Final configuration for Set No. 3 runs (V = 1.5 km/s, L/D=20).

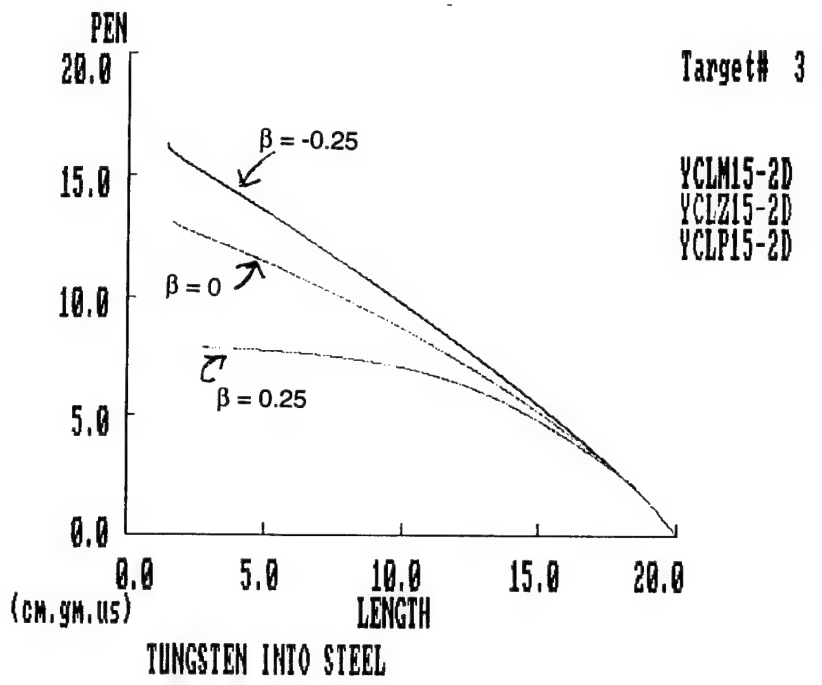

Figure 12. Penetration-erosion curves for Set No. 3.

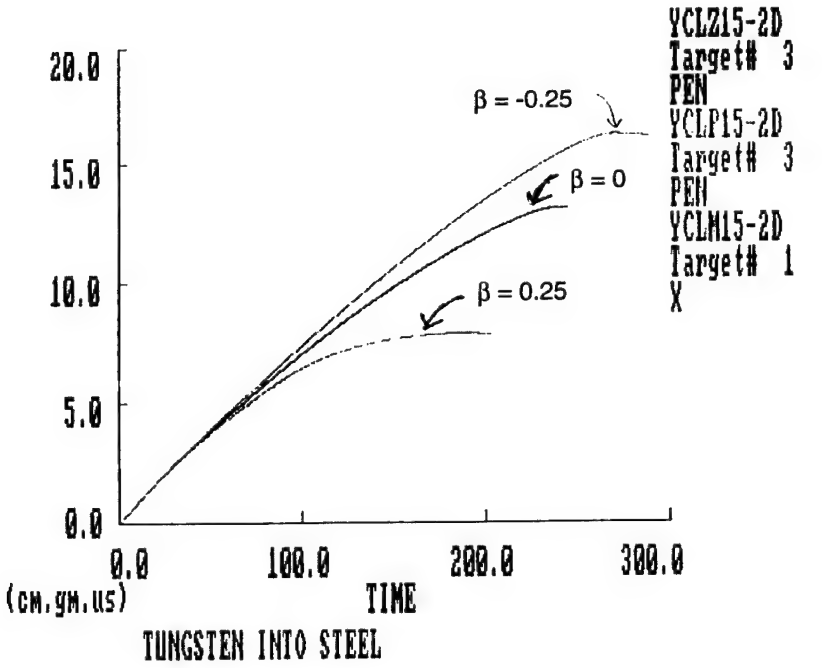

Figure 13. Penetration histories for Set No. 3.

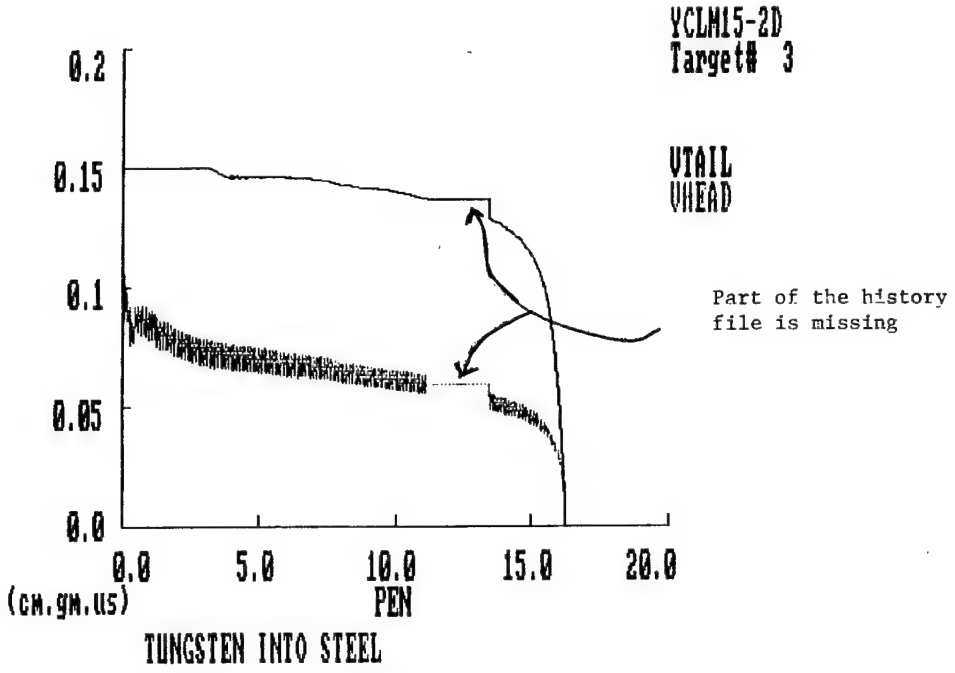

Figure 14.1. Interface velocity (VHEAD) and tail velocity (VTAIL) as a function of penetration (PEN) for β = -0.25 (Set No. 3).

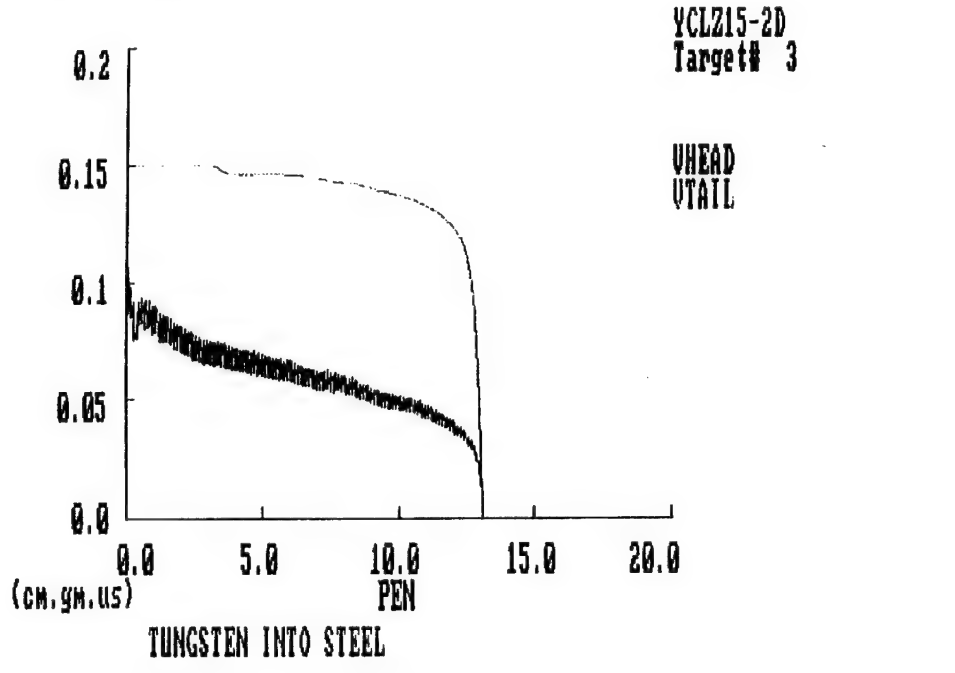

Figure 14.2. Interface velocity (VHEAD) and tail velocity (VTAIL) as a function of penetration (PEN) for β = 0 (Set No. 3).

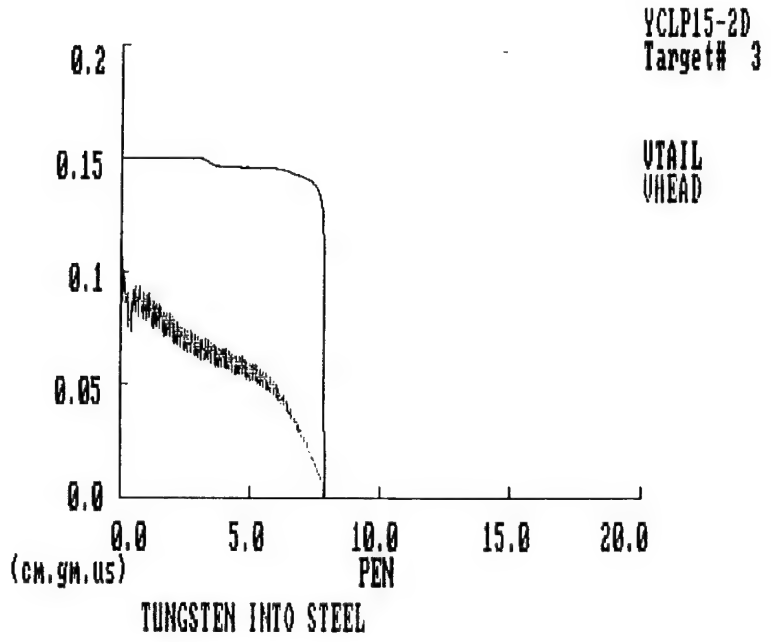

Figure 14.3. Interface velocity (VHEAD) and tail velocity (VTAIL) as a function of penetration (PEN) for $\beta = 0.25$ (Set No. 3).

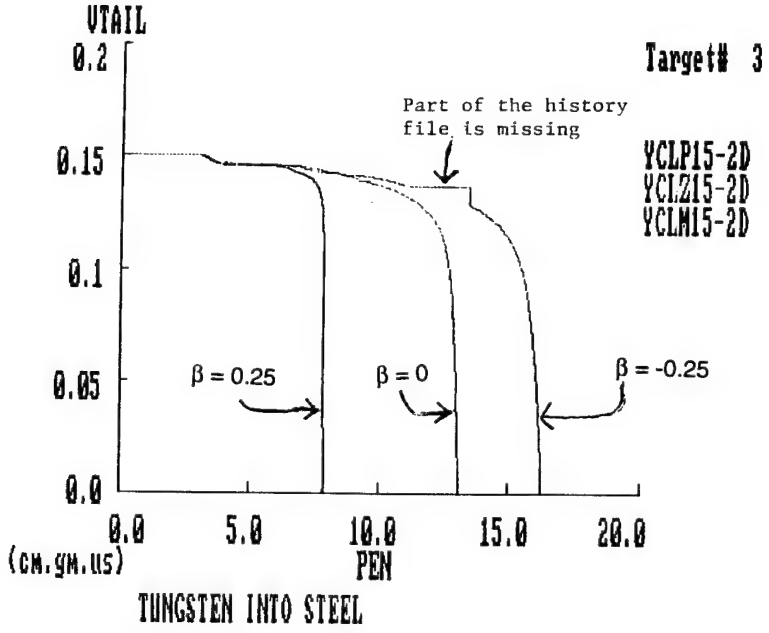

Figure 15. Tail velocity (VTAIL) as a function of penetration (PEN) for Set No. 3.

6. Set No. 4: Effect of a Strength Increase or Decrease

As explained in the Introduction, a strength increase can be regarded as a hardening/softening law that is different from the linear hardening used in Sets 1, 2, and 3. We are using this particular law (stress increase) because it includes as a special case the strain to failure model that is sometimes employed to describe failure of metals by shearbanding. We anticipate that the projectile-flow effect does not depend on a particular hardening/softening law, but only on the material being hard/soft as it flows.

To show this, we ran six simulations at 1.5 km/s and L/D=10, as outlined in Table 7 (Set 4a); and five simulations with Y = const., as outlined in Table 8 (Set 4b).

Table 7
Penetration Efficiencies for Set No. 4a

Y_o (GPa)	ε_j	Y_j(GPa)	P/L
2	1	0	1.037
2	1	4	0.516
2	1	0	0.915
2	2	0	0.909
1	1	0	0.990
0	1	1	0.834

Table 8
Penetration Efficiencies and Residual Projectile Length for Set No. 4b

Y(GPa)	P/L	L_f/L
0	0.855	0.043
1	0.912	0.089
2	0.809	0.143
3	0.660	0.211
4	0.498	0.257

The results of a strength change from Y_o = 2 GPa, at $\varepsilon^p_{eff} = \varepsilon_j = 1$ ($\equiv 100^{\circ}$ are shown in Figure 16. We see that as for linear hardening/softening (Set No. an increase in projectile strength leads to less penetration and a decrease to more ne-tration.

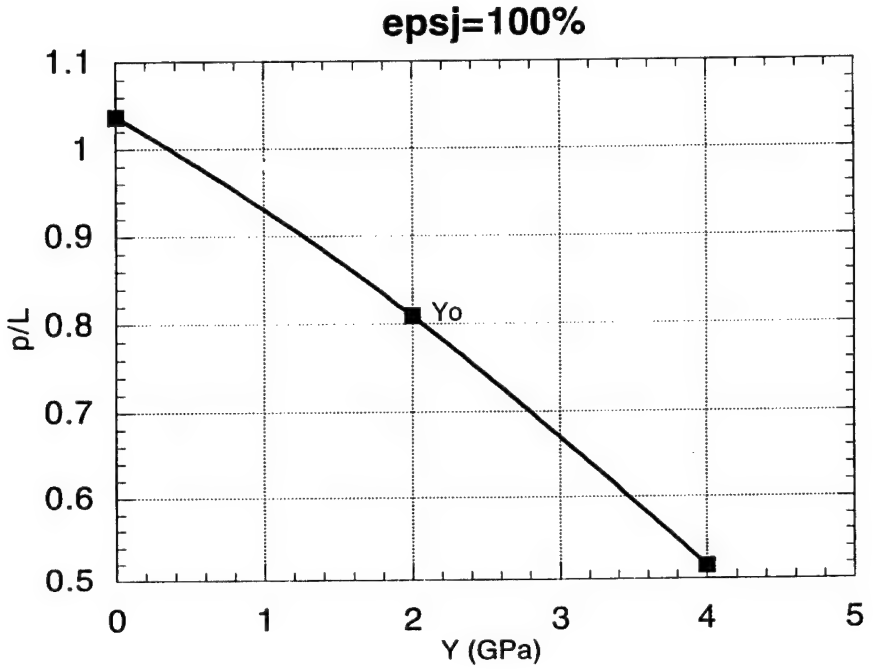

Figure 16. Penetration efficiency for a strength change from Y_o = 2. GPa, at ε^p_{eff} = 100%. Y_j is the strength after the change.

In Figure 17, we show the results of two runs with the same strength change (from 2 GPa to zero), but with different values of ε_j (100 and 200%). We see that for a strength change at a higher plastic strain value the penetration efficiency is lower.

It seems that the projectile-flow effect depends essentially on the projectile strength while it flows. It therefore has to manifest itself even for a constant strength projectile. To see this we ran Set 4b with different values of constant Y.

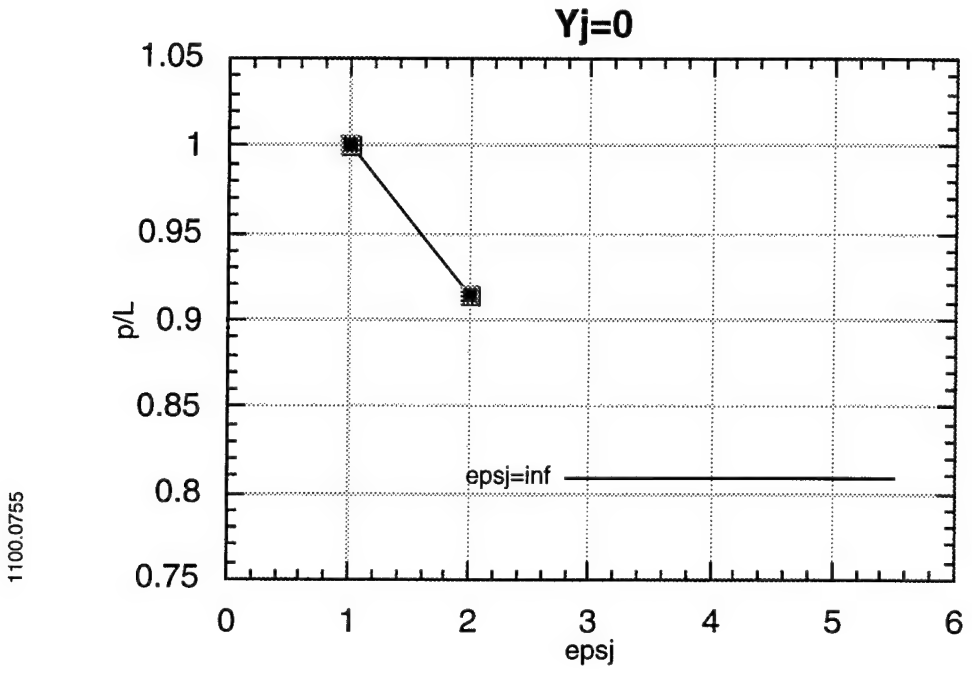

Figure 17. Penetration efficiency for a strength change from 2 GPa to zero at different values of ε_j.

Penetration efficiency results for constant Y runs are shown in Figure 18. We see that for low values of Y, P/L increases with Y, as expected based on Tate's model (i.e., penetration velocity decreases with R_t - Y_p; as Y increases, penetration velocity and also penetration efficiency are expected to increase.) But the P/L vs Y curve reaches a maximum at about Y = 1 GPa, and then decreases quite significantly. Rosenberg and Dekel [6], investigating the L/D effect at large L/D, calculated P/L (L/D) curves for Y = 0 and Y = 1.25 GPa. For L/D=10, they discovered that P/L (Y = 1.25) > P/L (Y = 0), in agreement with our results. But their curves cross over at about L/D=28. This would show that as L/D increases, the peak in the P/L vs Y curve moves to the left until, at some value of L/D ($\cong$ 28), it reaches Y = 0, and beyond that P/L only decreases.

In Figure 19, we show the results of Set 4b in terms of penetration-erosion curves. We see that initially the slopes (s = -dP/dL) are arranged according to strength (slope increases with strength), as expected from Tate's model.

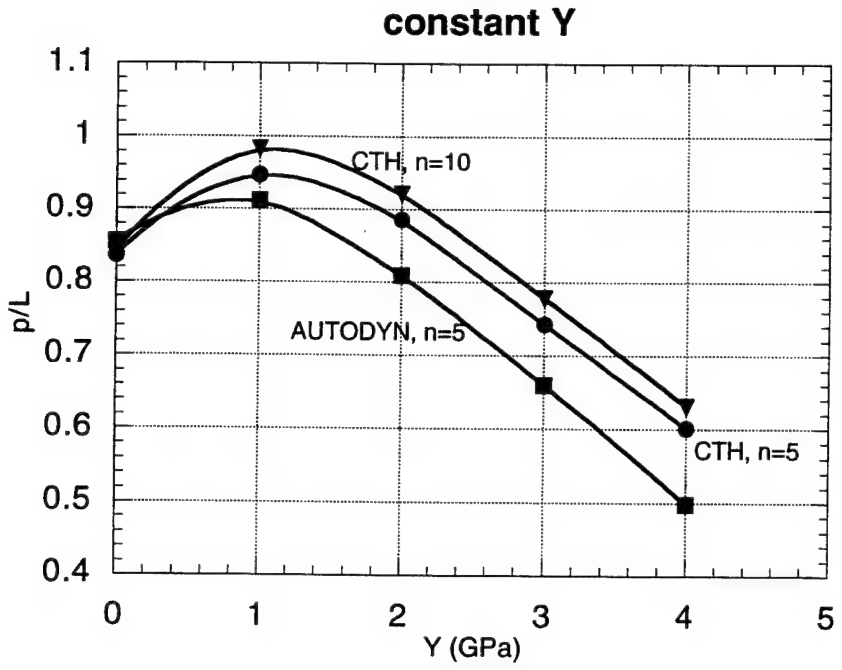

Figure 18. Penetration efficiency results for constant Y runs (Set 4b). n = number of cells across the projectile radius. "CTH" indicates results obtained with the CTH wavecode.

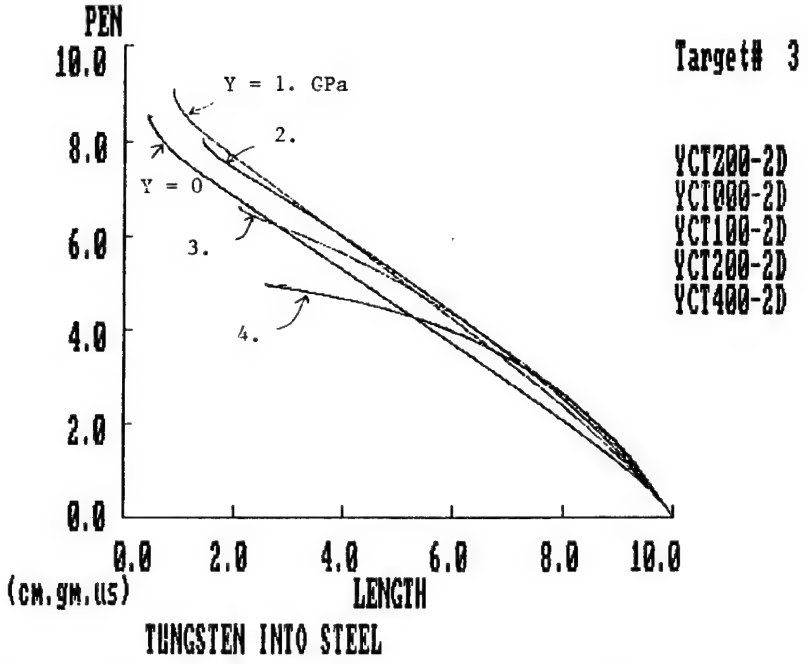

Figure 19. Penetration-erosion curves for constant Y Runs. L/D=10, V = 1.5 km/s.

But with increasing Y, the curves bend and tend to cross each other. The amount of bending increases with strength and is undoubtedly due to the projectile-flow effect. We also see that the residual projectile length (L_f) increases with Y. This is probably because at a higher strength the projectile flows more slowly and a larger part of it remains in the slug that is identified as the residual projectile. Values of L_f are given in Table 8 and shown in Figure 20. We see that L_f increases almost linearly with Y. In Figure 21, we show the penetration-erosion curve for the run with the strength change from Y_o = 2 GPa to Yj = 4 GPa at ε_j = 100%. As a reference, we also show in the figure the constant Y curves for Y = 2 and 4 GPa. We see that the curve starts off along the Y = 2 GPa curve, and then bends towards the Y = 4 GPa curve.

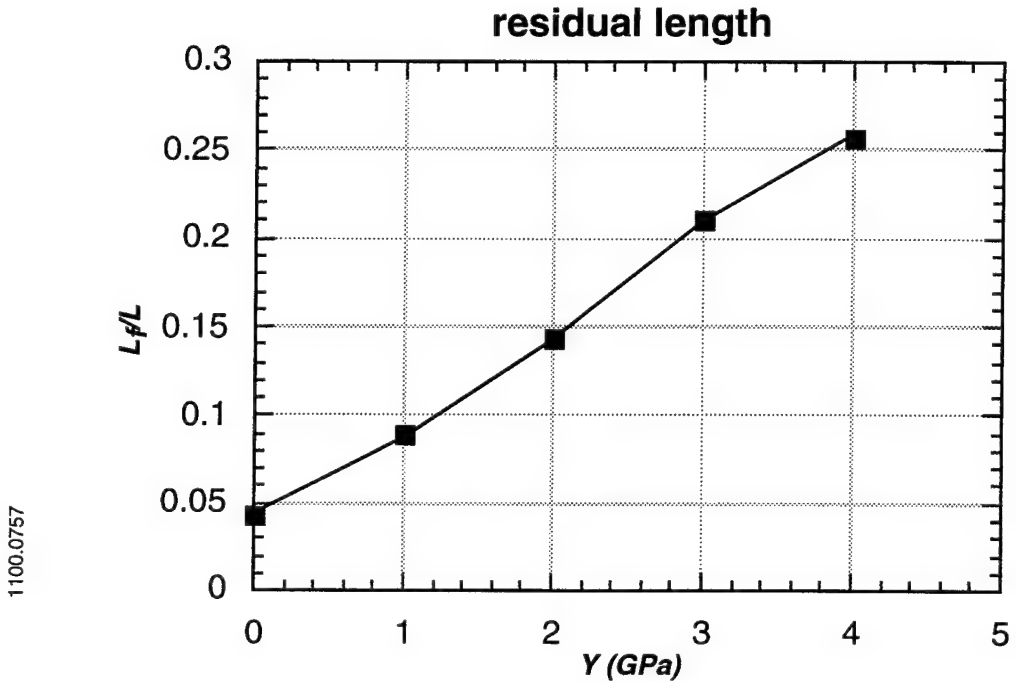

Figure 20. Relative residual projectile length L_f/L for constant Y runs.

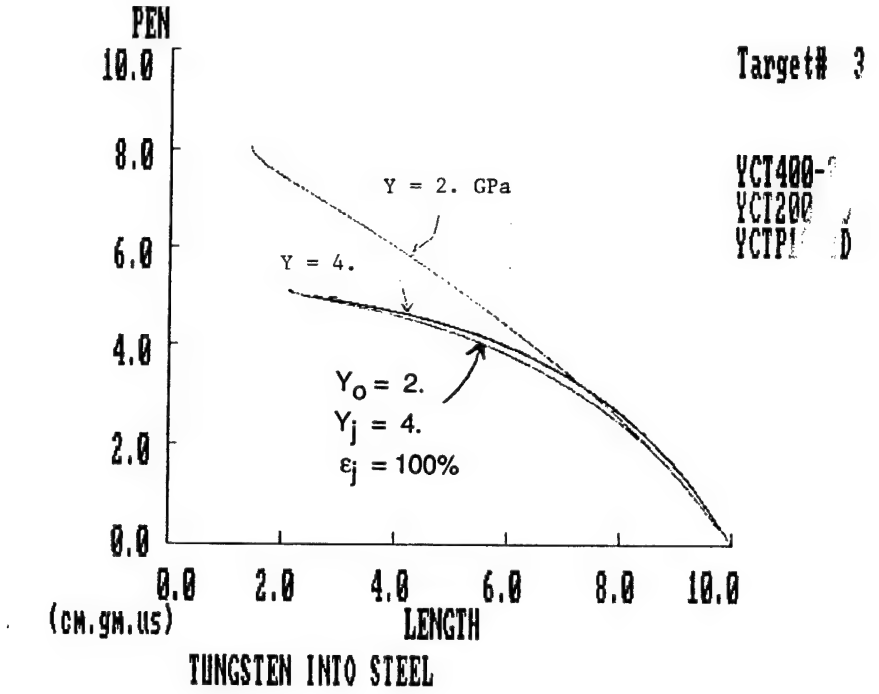

Figure 21. Penetration-erosion curves for the run with a strength change from 2 to 4 GPa, and for the constant strength runs with 2 and 4 GPa.

In Figure 22, we show penetration-erosion curves for the runs with $Y_j = 0$ (Set 4a). As a reference we also have the constant strength curves for Y = 0 and 2 GPa. We see that the curves with ε_j = 100 and 200% start the same as that with constant Y = 2 GPa, but then deviate upwards. The one with ε_j = 100% deviates first. This result is quite striking because the curves do not bend towards the Y = 0 curve, but in the opposite direction.

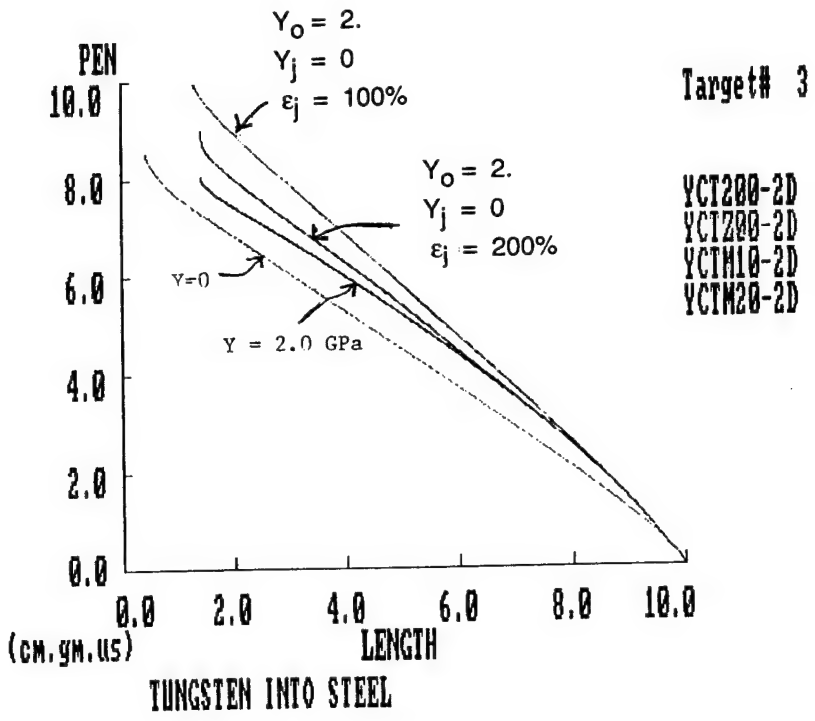

Figure 22. Penetration-erosion curves for the run with a strength change from 2 GPa to zero, and for constant strength runs with Y = 0 and 2 GPa.

In Figures 23 and 24 we show the results of the runs with a strength change from zero to 1 GPa, and from 1 GPa to zero, respectively.

These runs are of special interest as both Y = 0 and 1 GPa are on the upward part of the P/L vs Y curve in Figure 18. One may tend to assume that on the upward side the response would be reversed (compared to the downward side), but this is not the case.

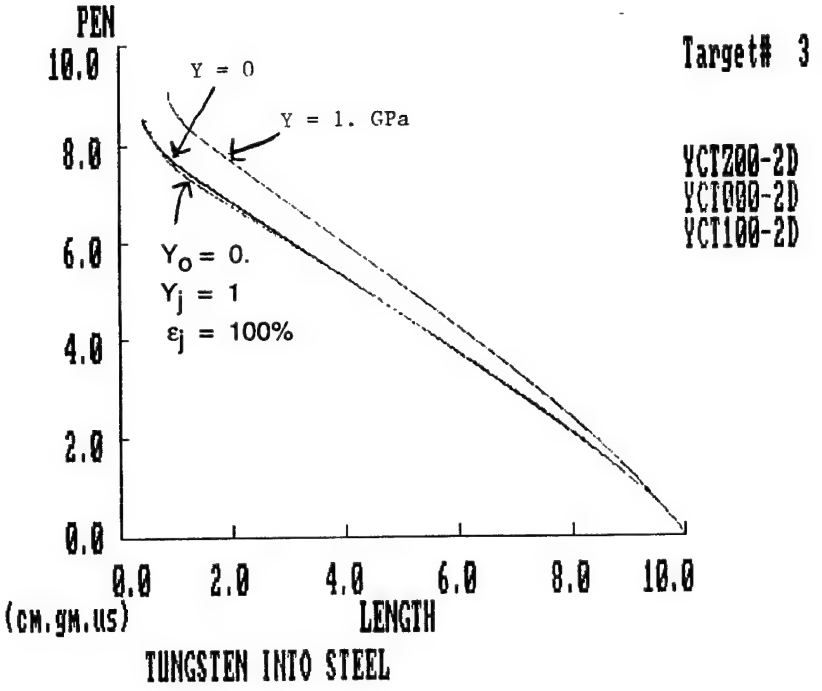

Figure 23. Results for a strength change from zero to 1 GPa.

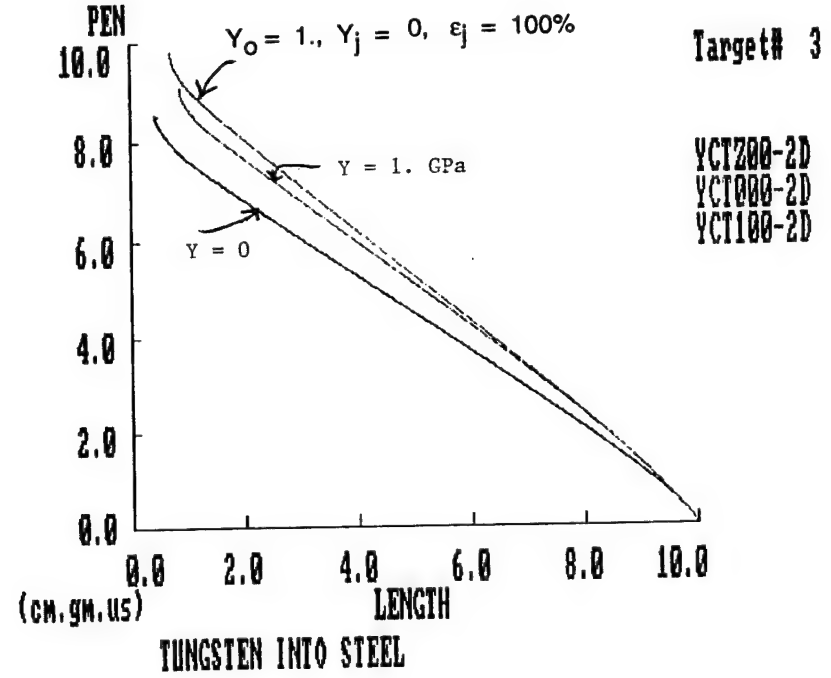

Figure 24. Results for a strength change from 1 GPa to zero.

7. Conclusions

We performed four sets of simulations with the Euler processor of AUTODYN to investigate the so called projectile-flow effect of long rod penetrators. According to common wisdom on long rod penetration based, for example, on the Tate model, penetration efficiency would increase slightly with projectile strength. Simulations show that this is not the case. Penetration efficiency depends significantly on the flow stress of the flowing projectile material. Moreover, the efficiency decreases/increases for a hardening/softening projectile material, respectively.

Computational Set No. 1 is for a linear hardening/softening material. We see that a hardening material cannot flow out of the way of the incoming projectile, thereby decelerating it. A softening material flows quickly out of the way, thereby increasing the penetration efficiency. Set No. 2 is the same as Set No. 1 but for a higher velocity. We see that the relative importance of the projectile-flow effect decreases with velocity. Set No. 3 is the same as 1 but for a higher L/D. We see that the projectile-flow effect is enhanced with L/D. It therefore seems that the projectile-flow effect is responsible for the L/D effect at large L/D [7]. Set No. 4 includes constant flow stress runs with Y = 0, 1, 2, 3, and 4 GPa, and runs with a strength change (up and down) at some effective plastic strain.

It is evident from these runs that the projectile-flow effect is active not just when there is hardening or softening, but also when the flow stress is constant. The magnitude of the effect is determined by the level of the flow stress in the flowing projectile.

From the strength change calculations, we see again that the projectile-flow effect does not depend on a specific hardening/softening law but only on the flow stress level in the flowing projectile.

Acknowledgment

This work was supported by the U.S. Army Armament Research, Development and Engineering Center (ARDEC) under contracts DAAA21-90-D-0009 and DAAA21-93-C-0101.

References

[1] L. Magness, "Deformation behavior and its relationship to the penetration performance of high density KE penetrator materials," Army Science Conference, Raleigh, NC, 1990.

[2] W. J. Bruchey, et al., "Orientation dependence of deformation and penetration behavior of tungsten single-crystal rods," Proceedings of the 120th TMS Annual Meeting on Recent Advances in Tungsten and Tungsten Alloys Conference, New Orleans, LA, Feb 17-21, 1991.

[3] Y. Partom and D. Yaziv, "Penetration of L/D=10 and 20 tungsten alloy projectiles into RHA targets," Shock Waves in Condensed Materials, Colorado Springs, CO, 1993.

[4] J. Reaugh, "Computer simulations to study the effect of adiabatic heating on rod penetration," Ballistics '93, 14th Int. Symp,. Quebec City, vol. 2, p. 505, 1993.

[5] Y. Partom, "Comparison of penetration efficiency in axial and planar symmetries," IAT.R 0033, November 1993.

[6] Z. Rosenberg and E. Dekel, "The relation between the penetration capability of long rods and their length to diameter ratio," *Int. J. Impact Engrg.*, vol. 15, p. 125, 1994.

[7] C. E. Anderson, et al., "On the L/D effect for long rod penetrators," submitted to the *Int. J. Impact Engrg.*

Appendix A

Appendix A is added to this report for possible future reference to details of these runs. Appendix A gives plots extracted for the seven runs of Set No. 1. The plots given for each run (except for $\beta = 0$) are:

- penetration-erosion curve (PL)
- interface velocity and tail velocity histories
- material status every 400 cycles
- velocity vectors near the interface every 400 cycles
- effective plastic strain contours every 400 cycles

The different runs are named as follows:

Run Name	β
A1	-0.25
A2	-0.10
A3	0
A4	0.10
A5	0.25
A6	0.50
A7	1.00

where β is the hardening/softening coefficient defined by Eq. (1) in the Introduction.

Appendix A1

β = -0.25

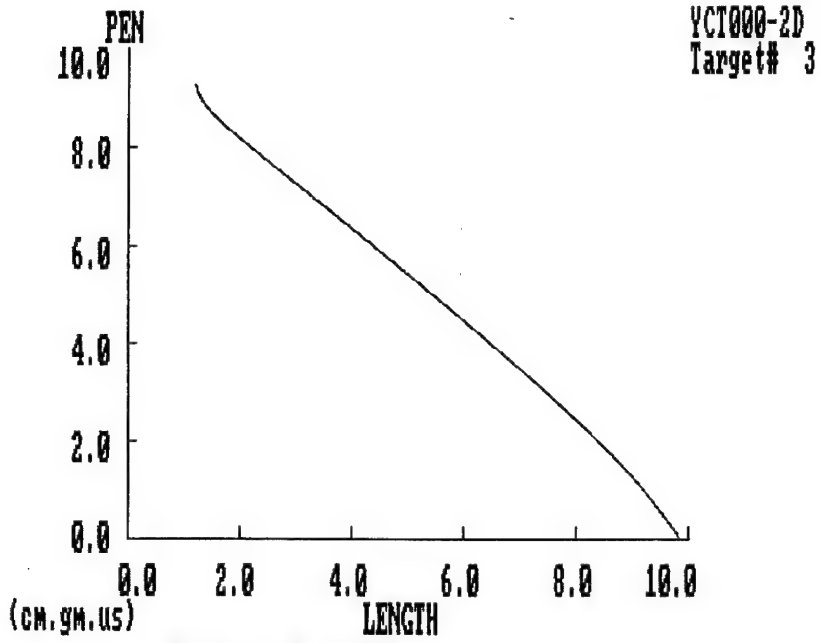

TUNGSTEN INTO STEEL

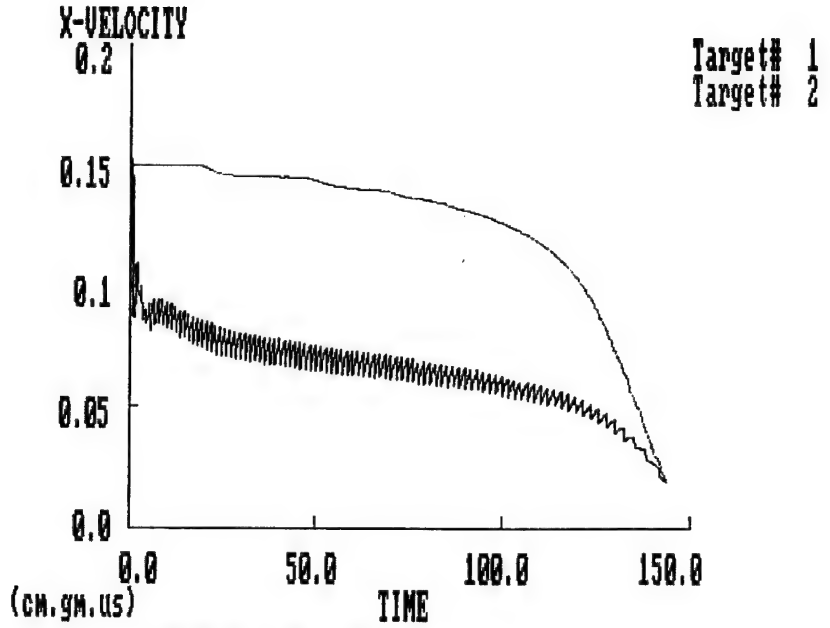

TUNGSTEN INTO STEEL

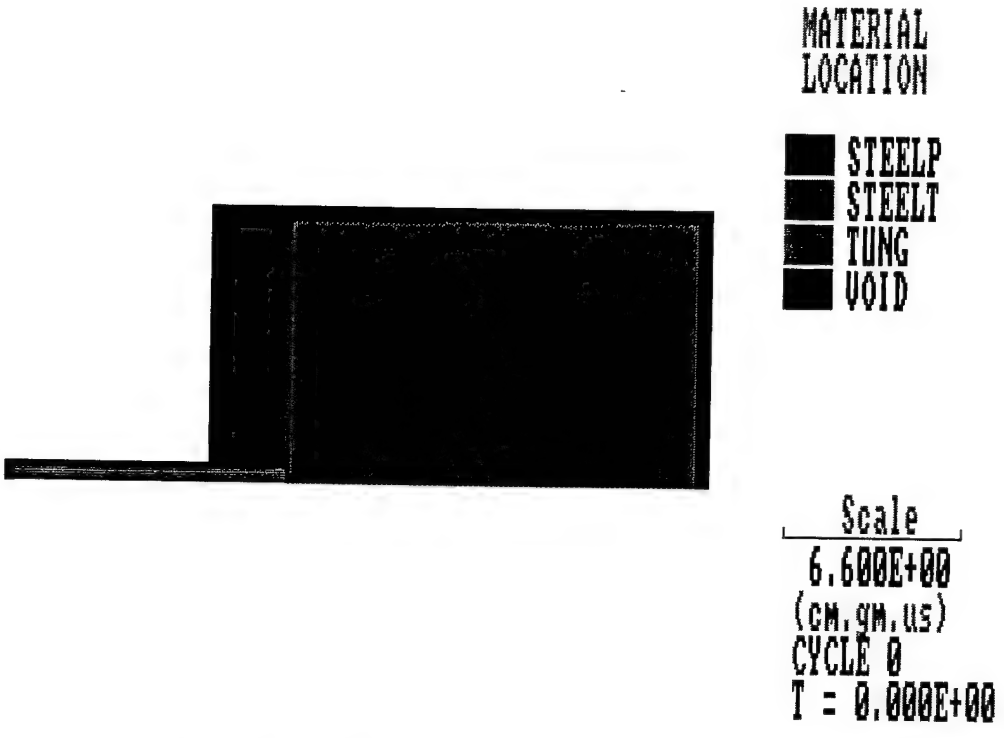

TUNGSTEN INTO STEEL

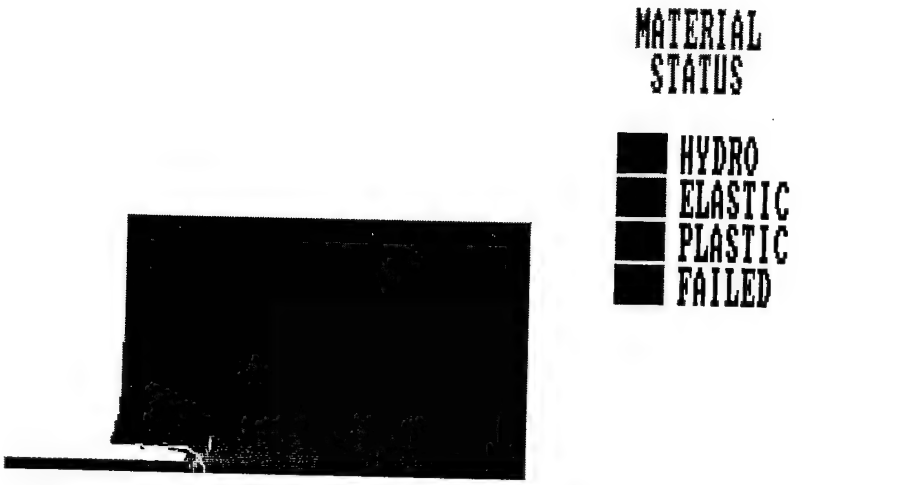

TUNGSTEN INTO STEEL

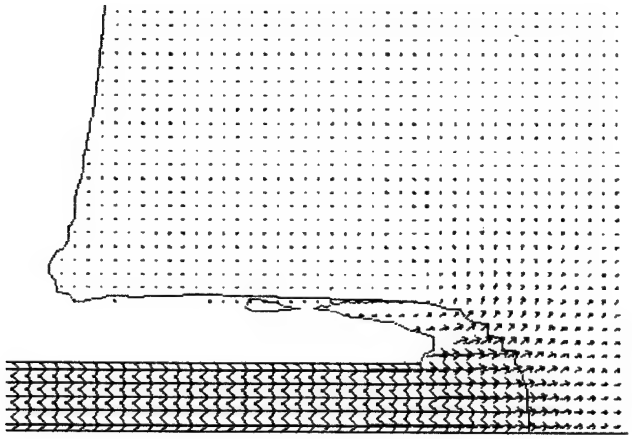

VELOCITY
VECTORS

Scale

8.000E-01

Maximum
Velocity
1.476E-01

Scale
1.000E+00
(cm.gm.us)
CYCLE 400
T = 3.923E+01

TUNGSTEN INTO STEEL

EFF.PL.STN

1.60E+00
1.20E+00
8.00E-01
4.00E-01
0.00E+00

(cm.gm.us)
CYCLE 400
T = 3.923E+01

TUNGSTEN INTO STEEL

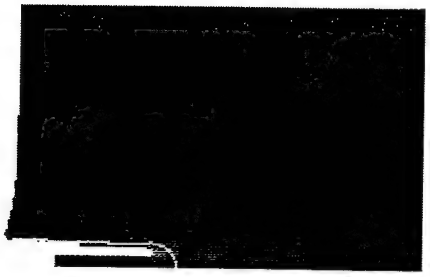

TUNGSTEN INTO STEEL

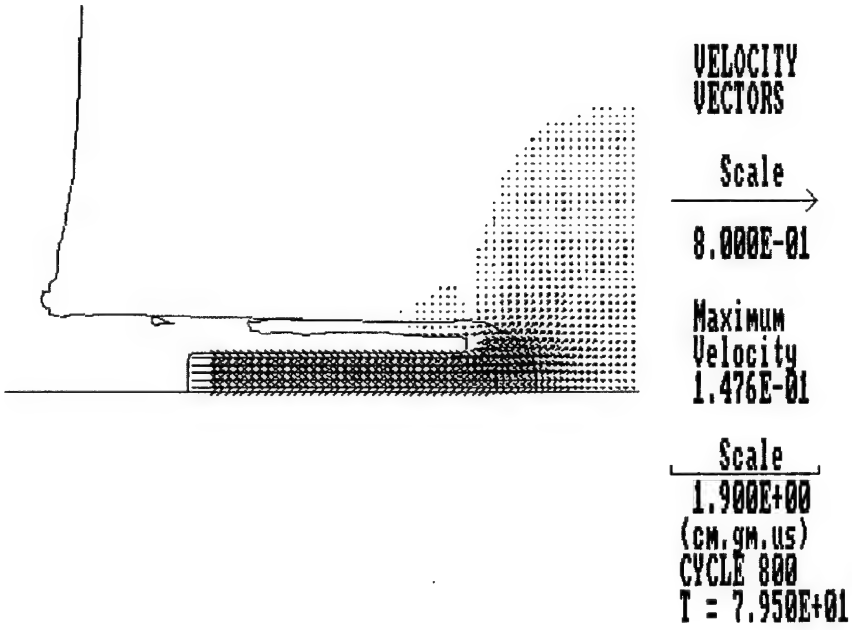

TUNGSTEN INTO STEEL

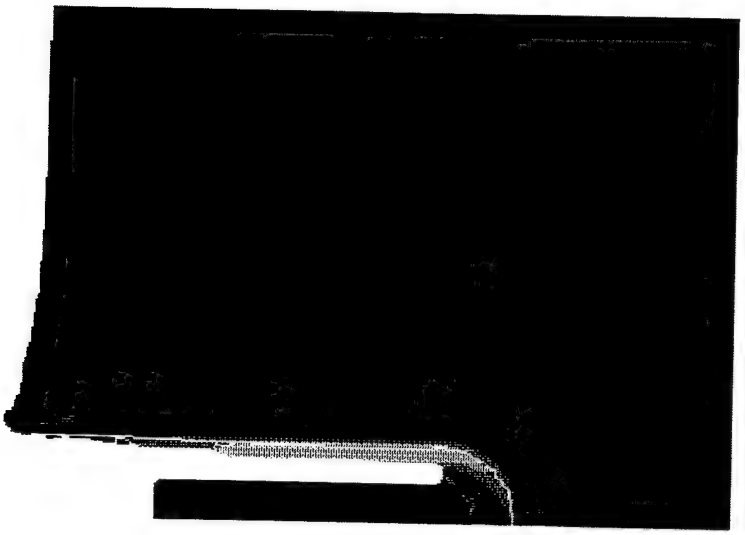

(cm.gm.us)
CYCLE 800
T = 7.950E+01

TUNGSTEN INTO STEEL

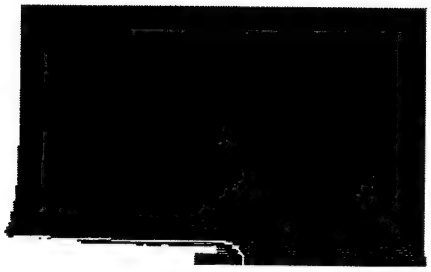

(cm.gm.us)
CYCLE 1200
T = 1.208E+02

TUNGSTEN INTO STEEL

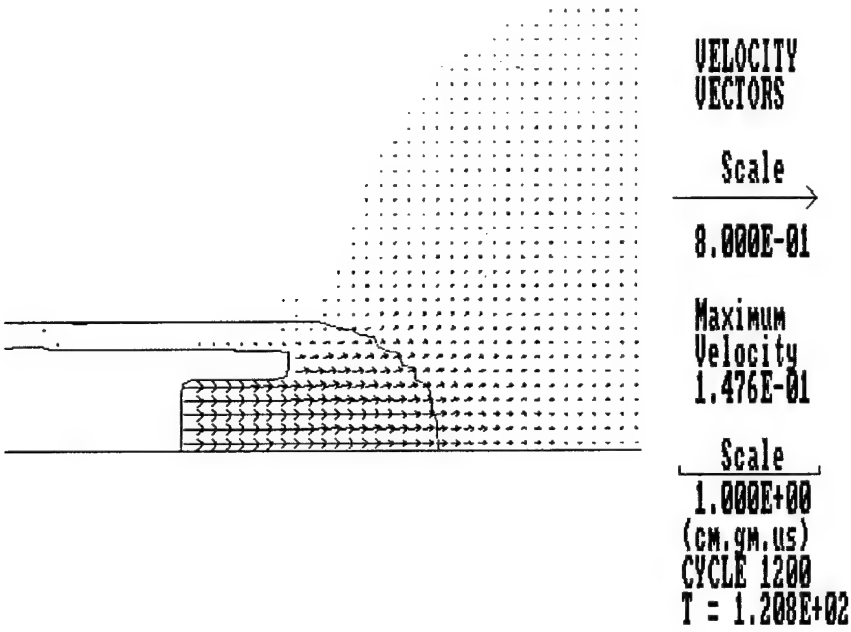

TUNGSTEN INTO STEEL

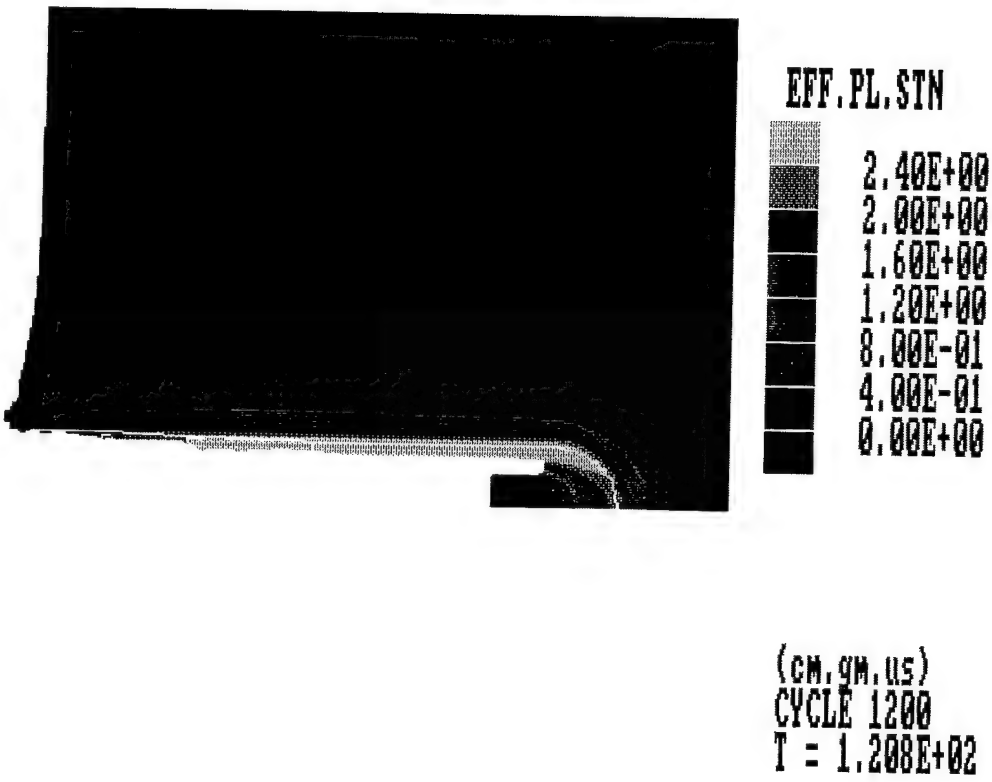

TUNGSTEN INTO STEEL

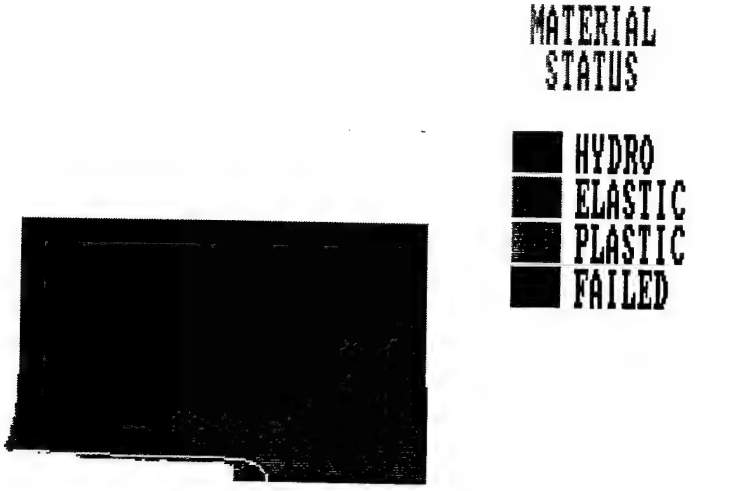

TUNGSTEN INTO STEEL

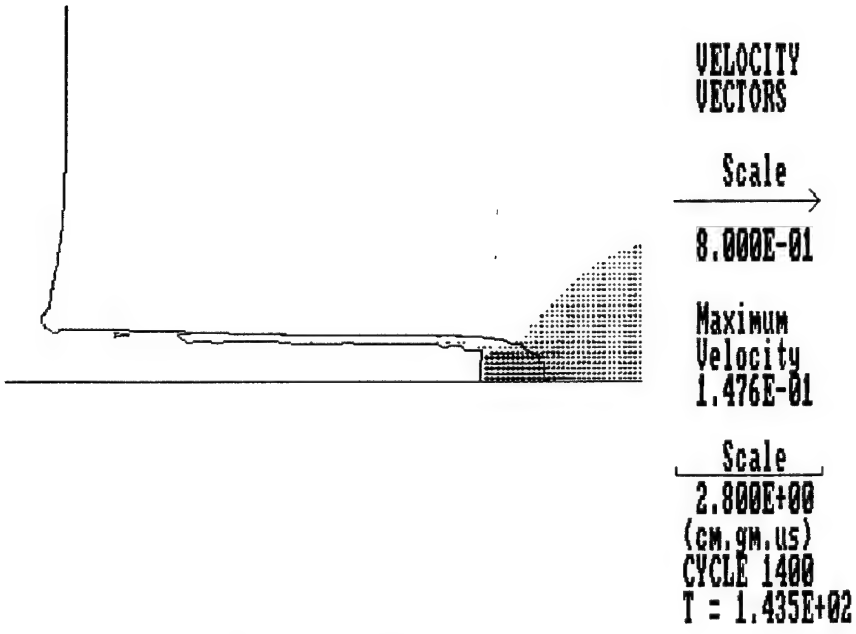

TUNGSTEN INTO STEEL

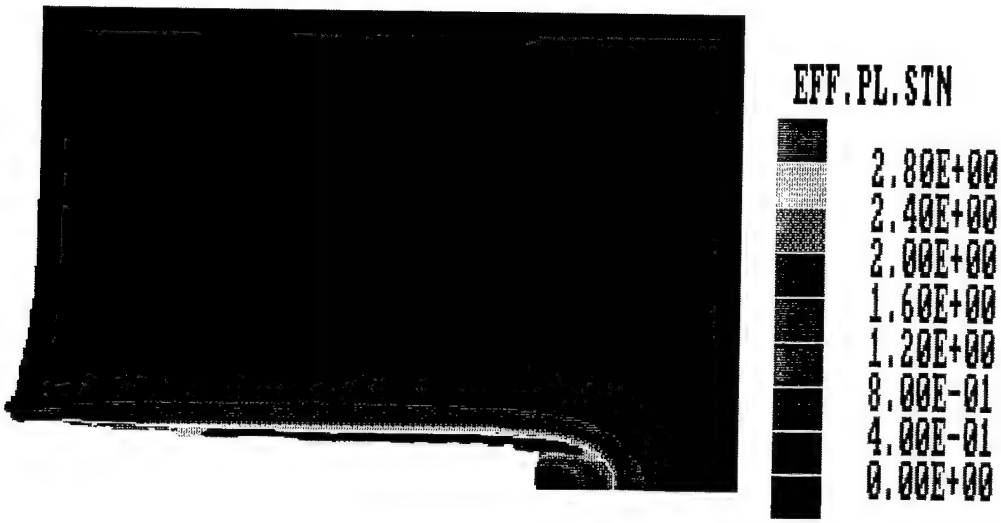

TUNGSTEN INTO STEEL

Appendix A2

β = -0.10

$\beta = \frac{B}{Y} = -0.1$

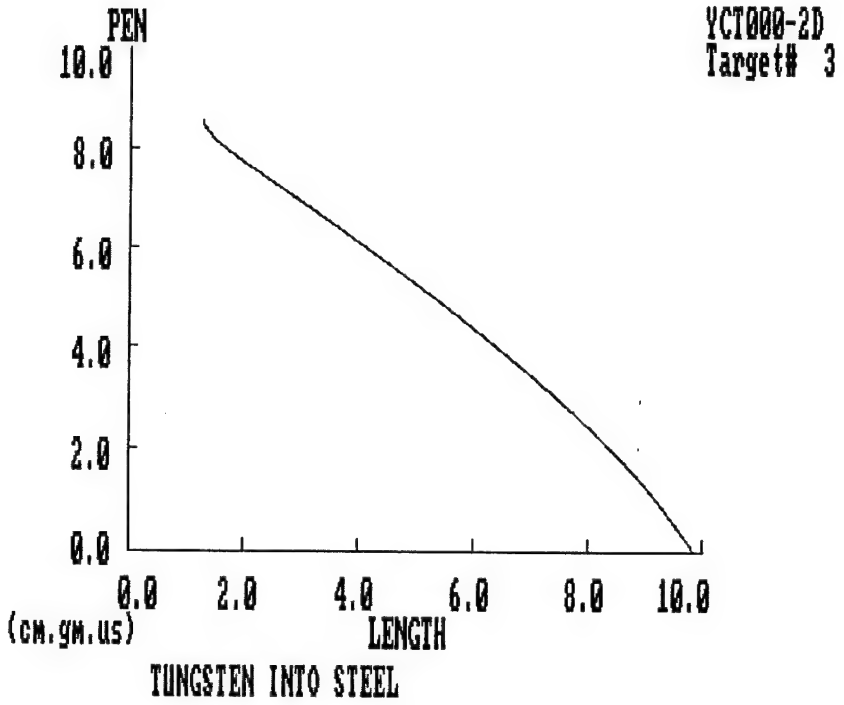

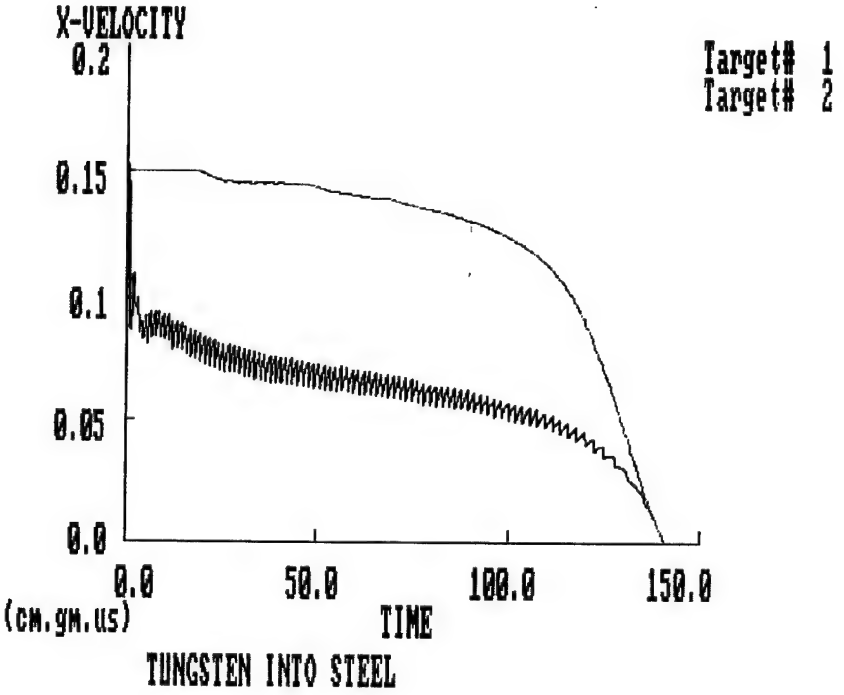

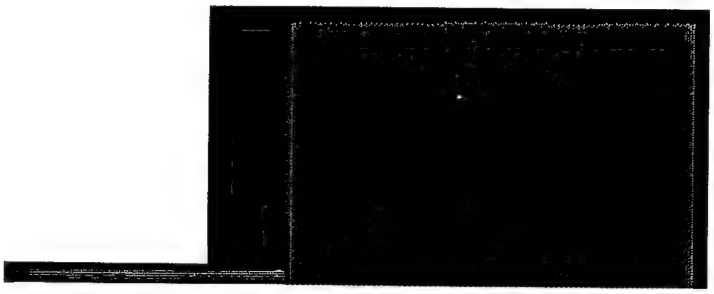

TUNGSTEN INTO STEEL

TUNGSTEN INTO STEEL

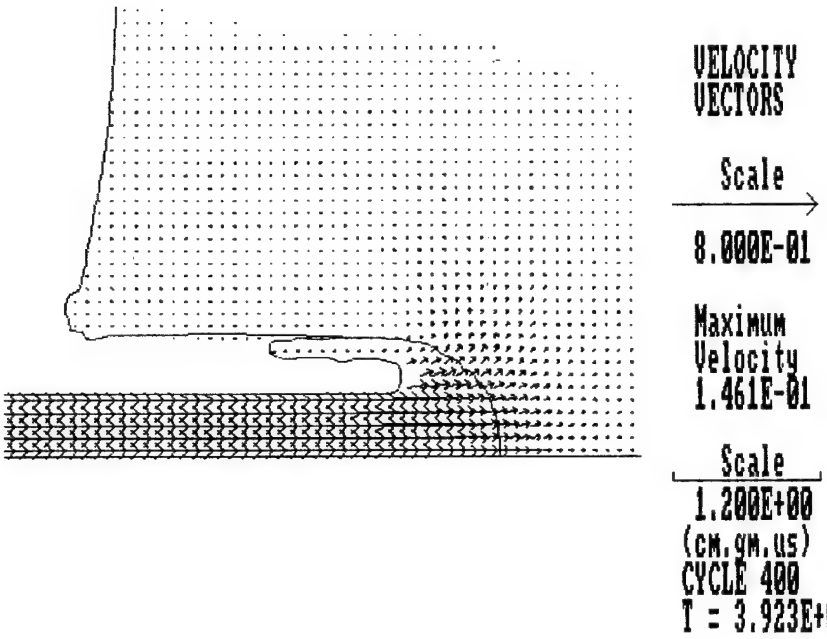

TUNGSTEN INTO STEEL

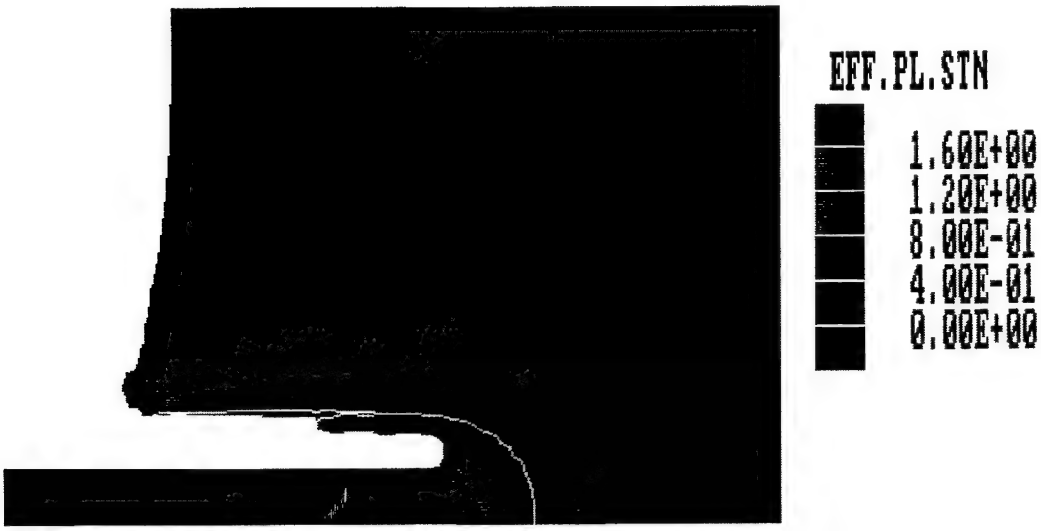

TUNGSTEN INTO STEEL

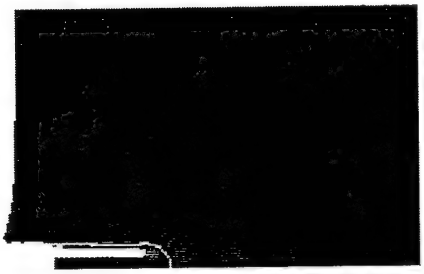

TUNGSTEN INTO STEEL

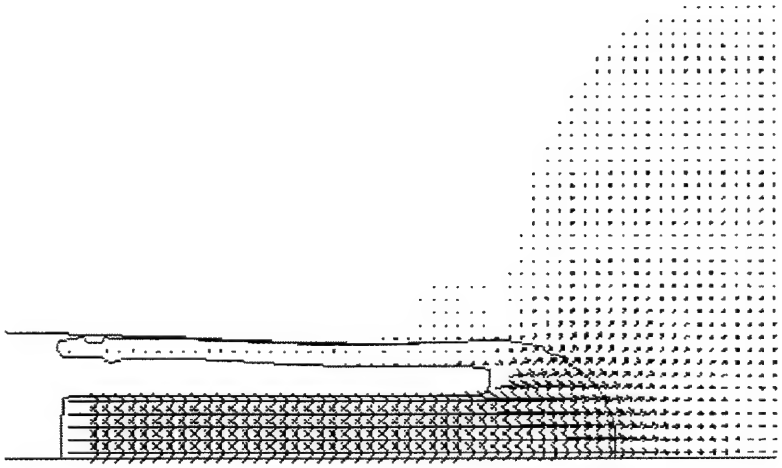

TUNGSTEN INTO STEEL

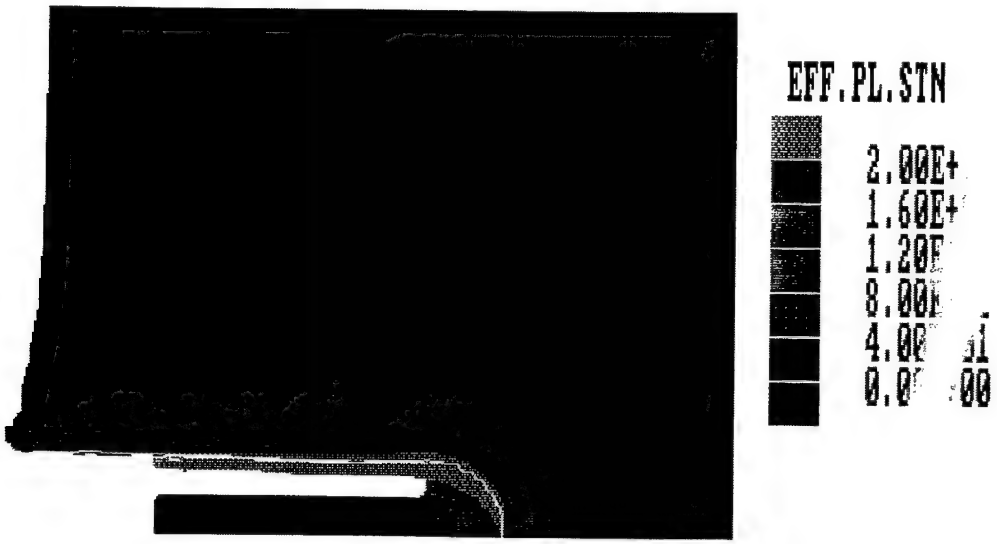

TUNGSTEN INTO STEEL

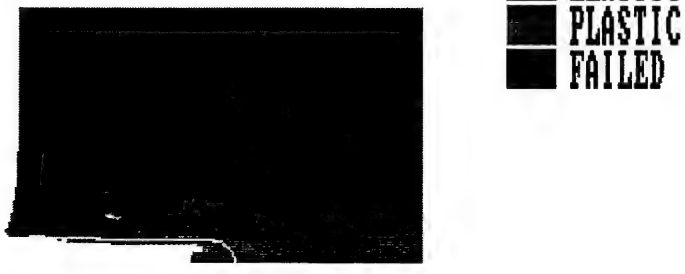

TUNGSTEN INTO STEEL

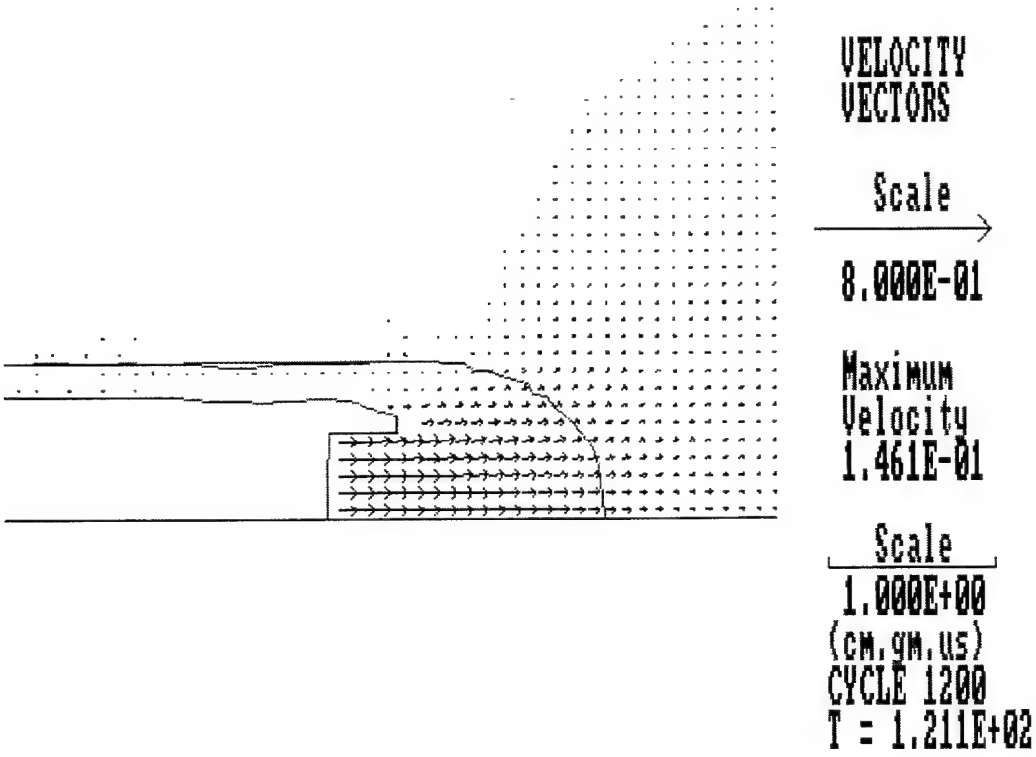

TUNGSTEN INTO STEEL

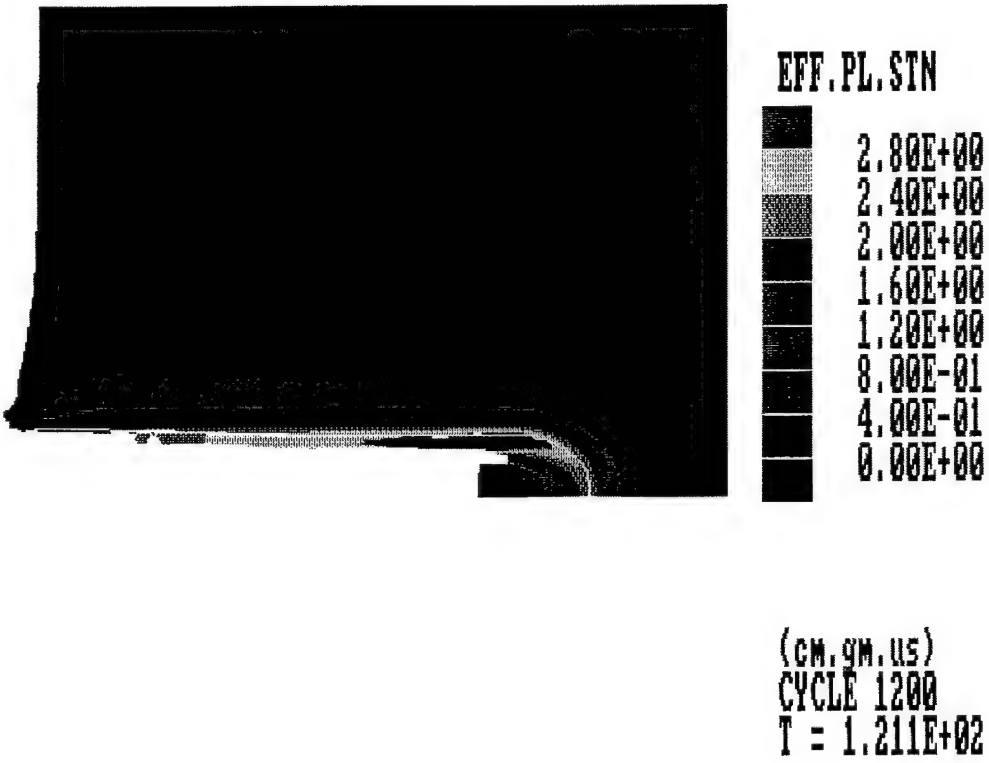

TUNGSTEN INTO STEEL

TUNGSTEN INTO STEEL

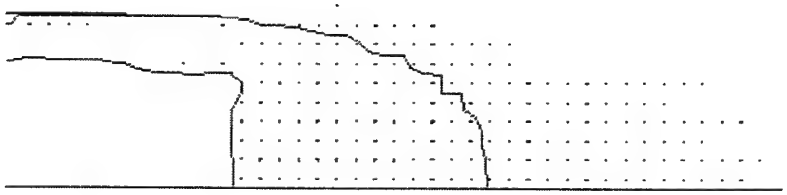

TUNGSTEN INTO STEEL

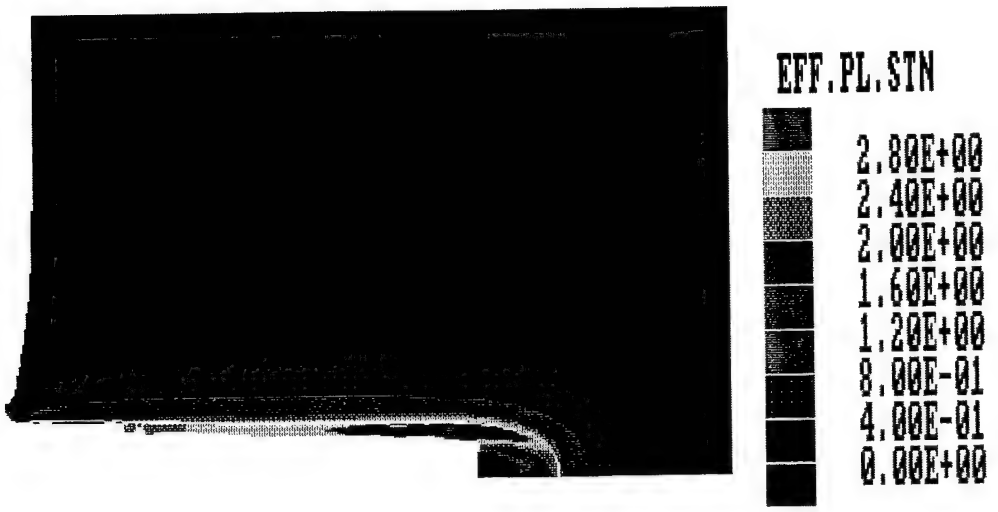

TUNGSTEN INTO STEEL

Appendix A3

$\beta = 0$ (constant flow stress)

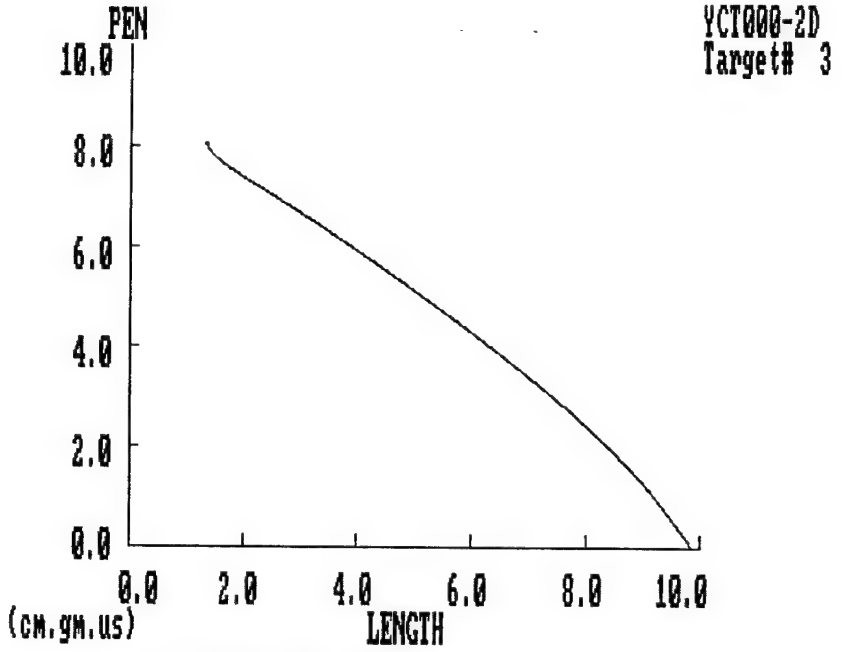
PEN
YCT000-2D
Target# 3
10.0
8.0
6.0
4.0
2.0
0.0
0.0
2.0
4.0
6.0
8.0
10.0
(cm,gm,us)
LENGTH
TUNGSTEN INTO STEEL

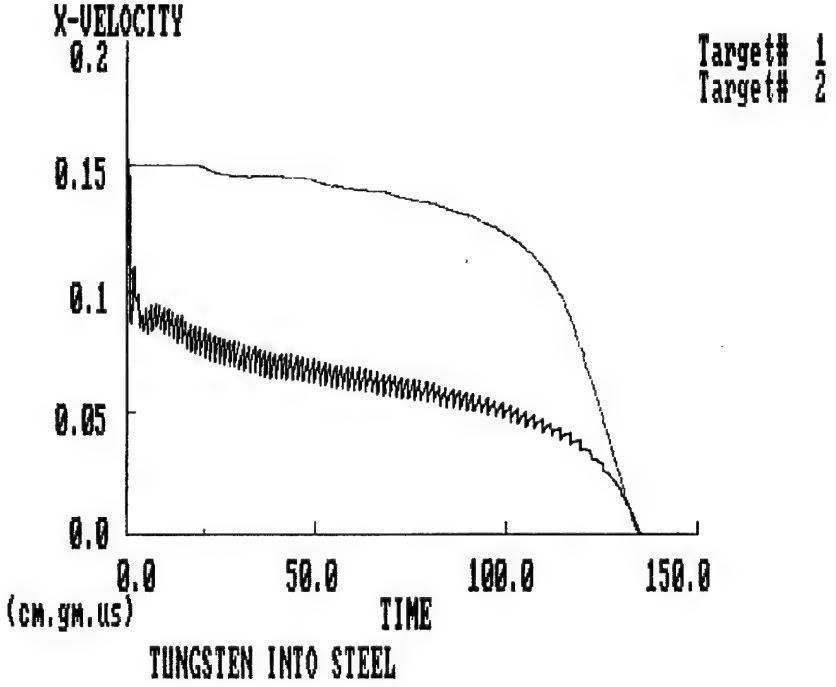
X-VELOCITY
Target# 1
Target# 2
0.2
0.15
0.1
0.05
0.0
0.0
50.0
100.0
150.0
(cm,gm,us)
TIME
TUNGSTEN INTO STEEL

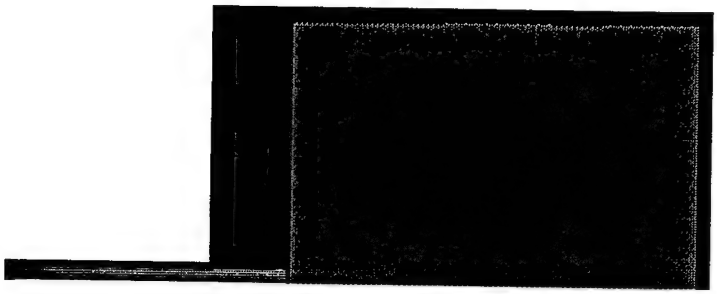

TUNGSTEN INTO STEEL

TUNGSTEN INTO STEEL

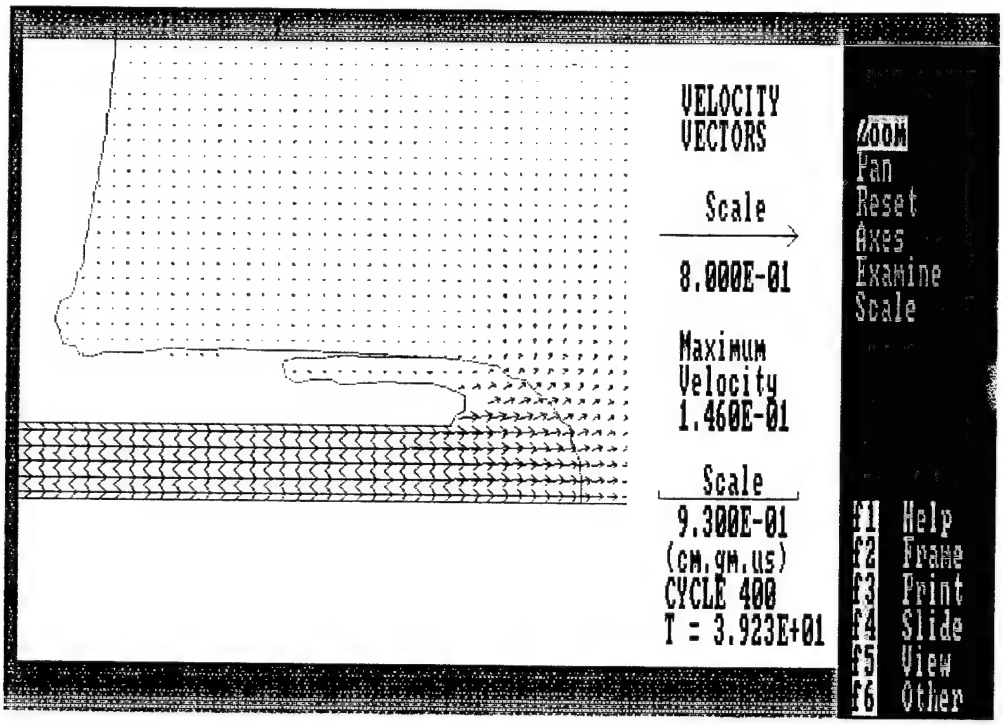

TUNGSTEN INTO STEEL

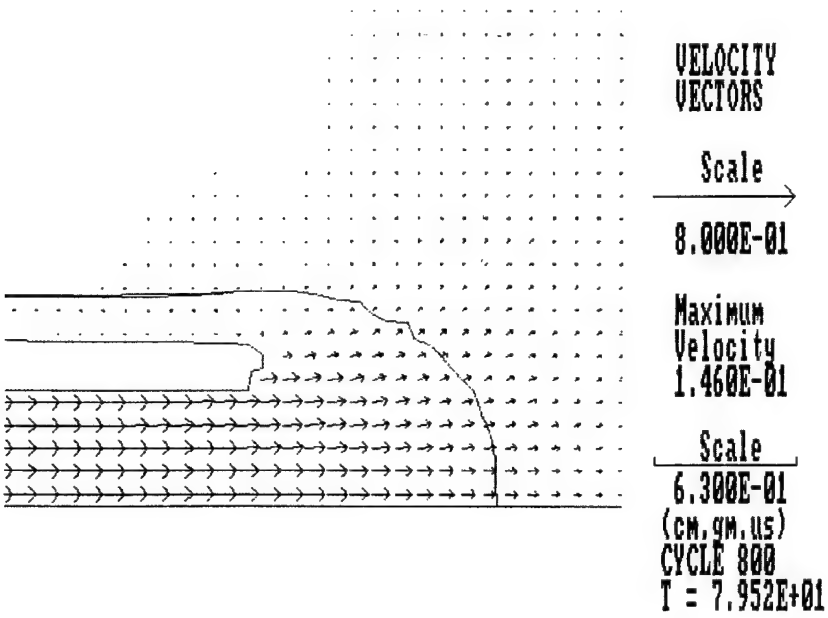

TUNGSTEN INTO STEEL

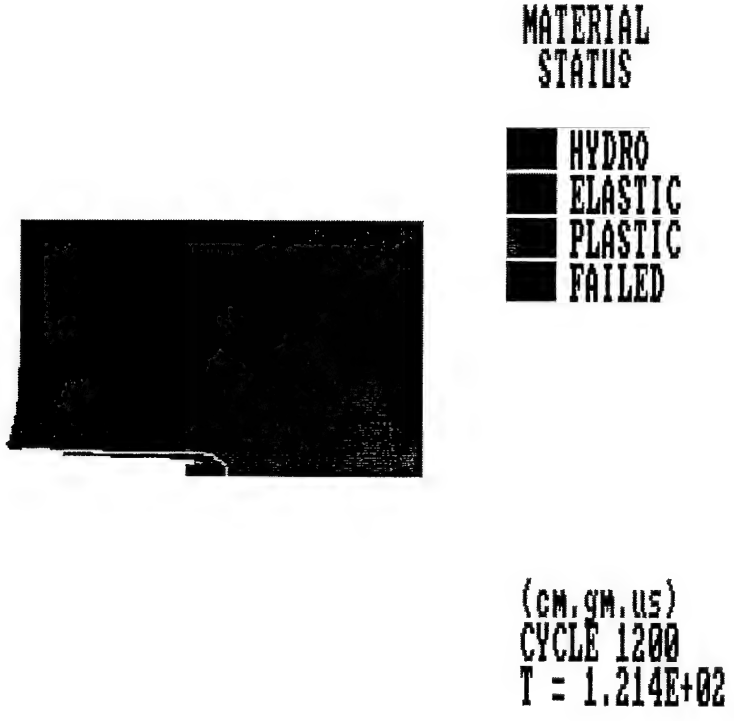

TUNGSTEN INTO STEEL

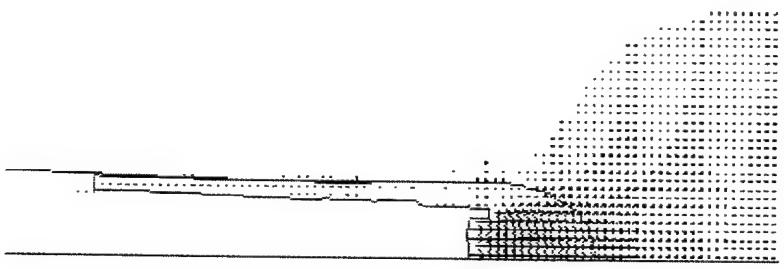

TUNGSTEN INTO STEEL

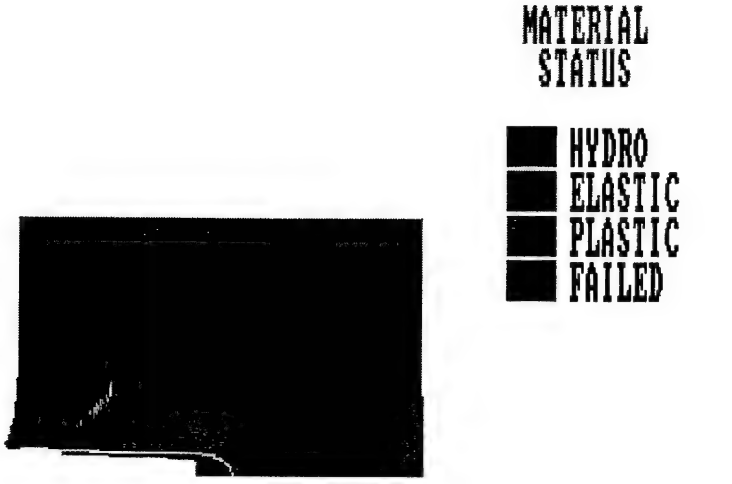

TUNGSTEN INTO STEEL

TUNGSTEN INTO STEEL

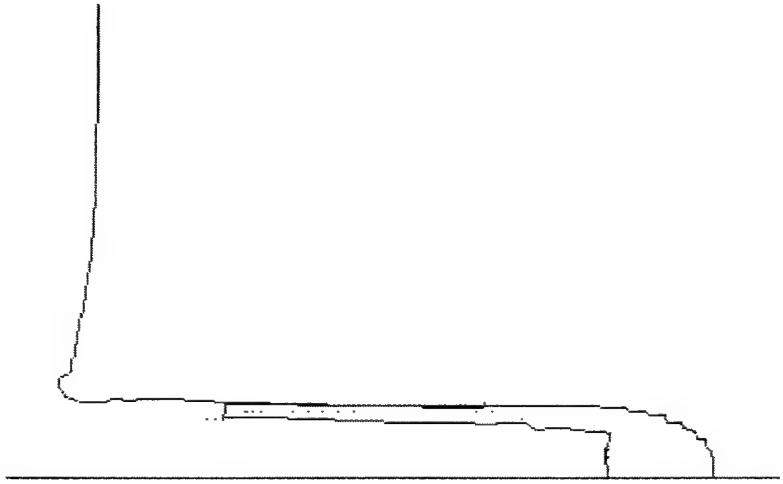

TUNGSTEN INTO STEEL

Appendix A4

$\beta = 0.10$

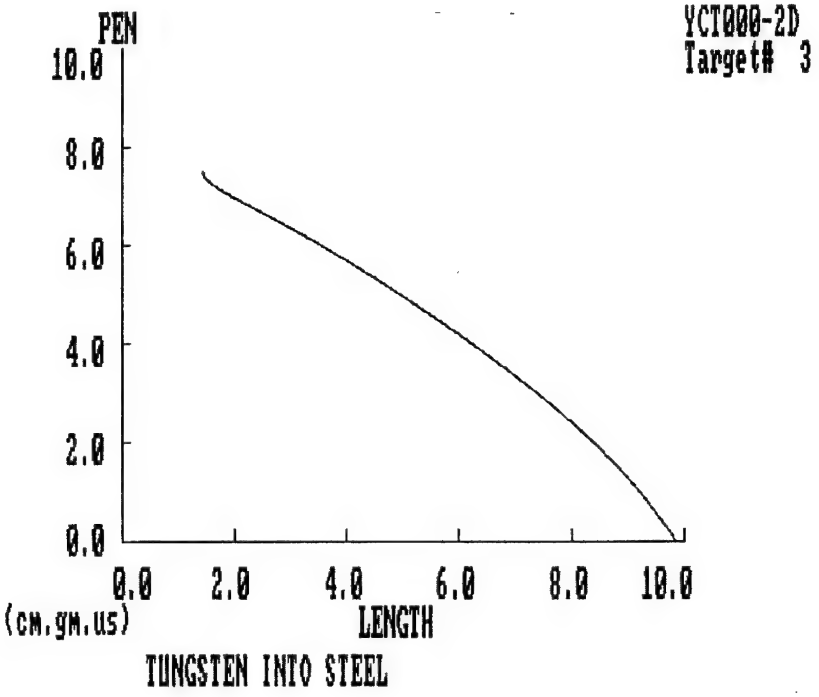
PEN
YCT000-2D
Target# 3
10.0
8.0
6.0
4.0
2.0
0.0
0.0
2.0
4.0
6.0
8.0
10.0
(cm,gm,us)
LENGTH
TUNGSTEN INTO STEEL

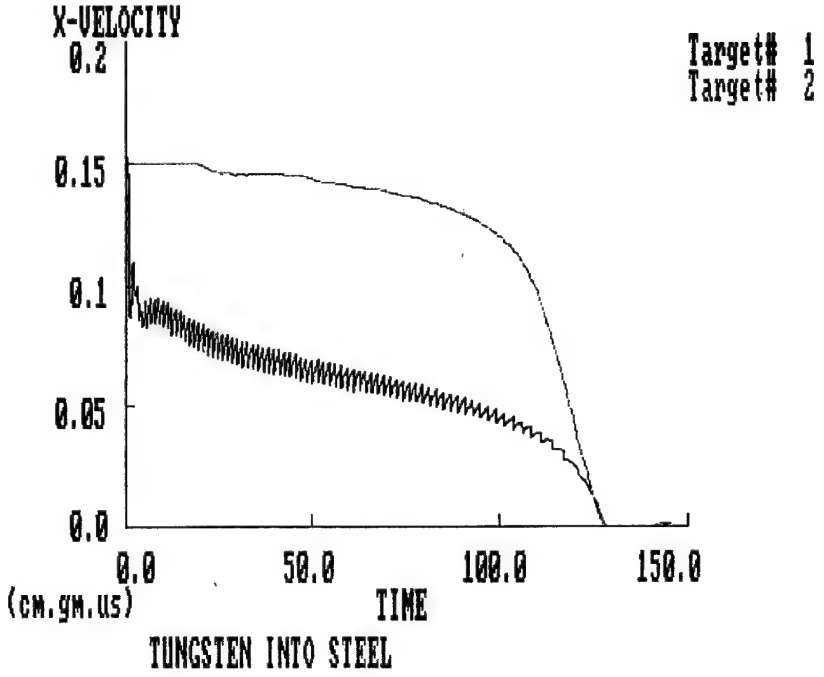
X-VELOCITY
Target# 1
Target# 2
0.2
0.15
0.1
0.05
0.0
0.0
50.0
100.0
150.0
(cm,gm,us)
TIME
TUNGSTEN INTO STEEL

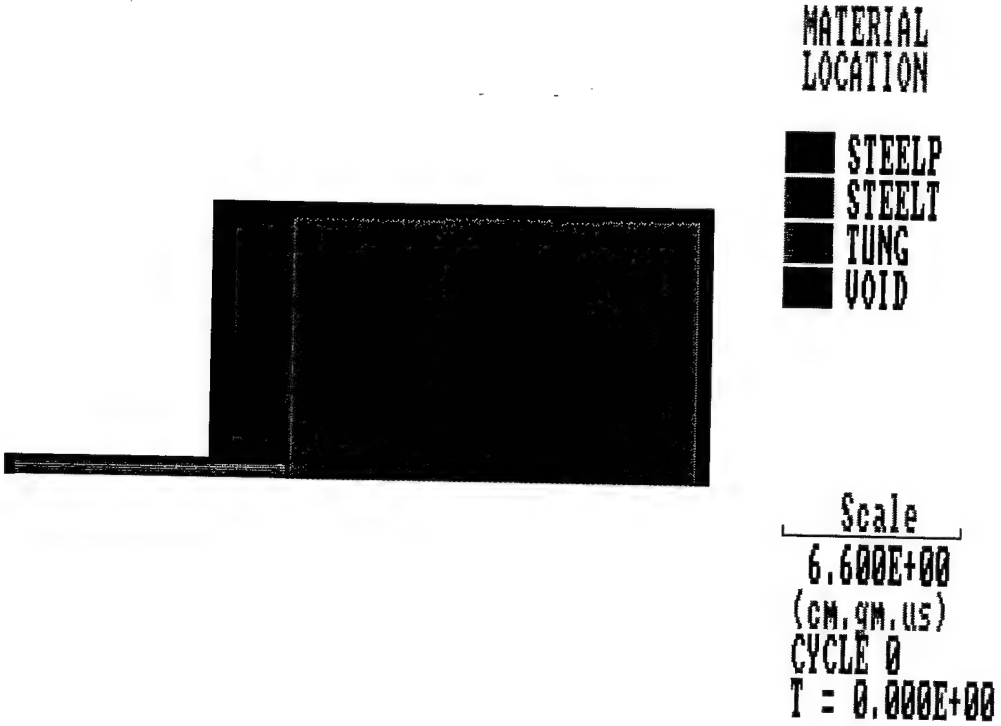

TUNGSTEN INTO STEEL

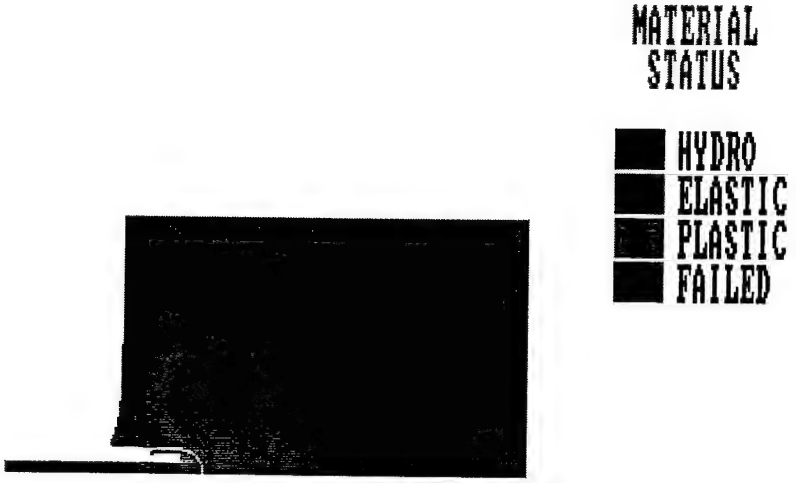

TUNGSTEN INTO STEEL

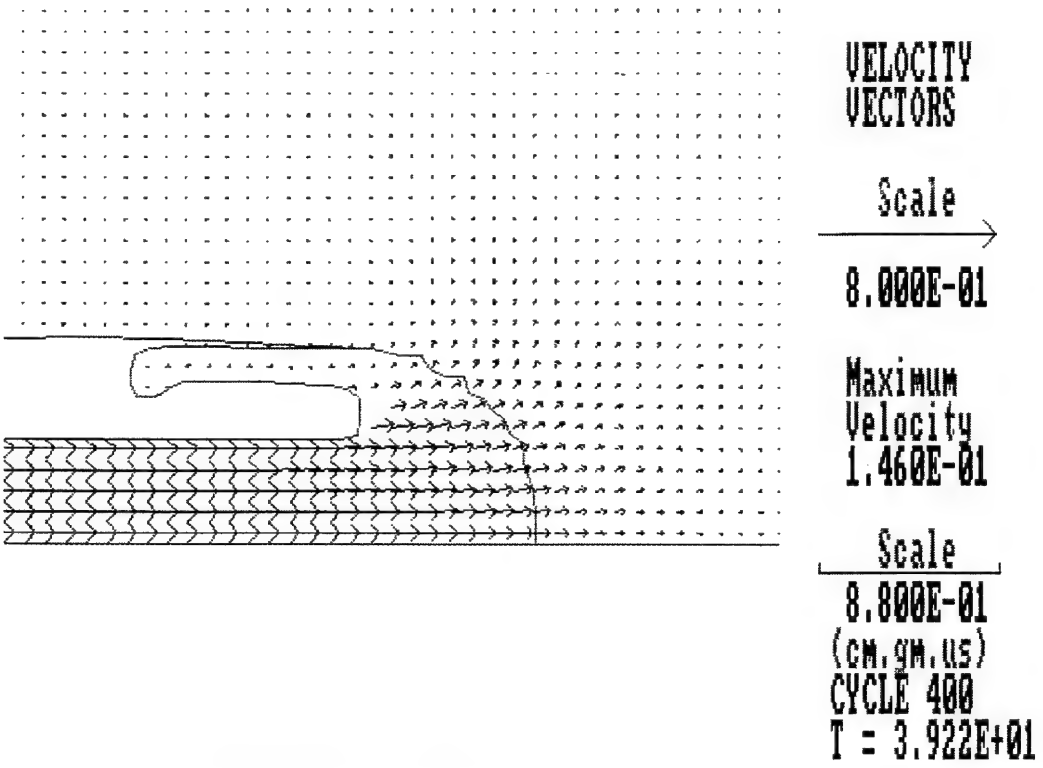

TUNGSTEN INTO STEEL

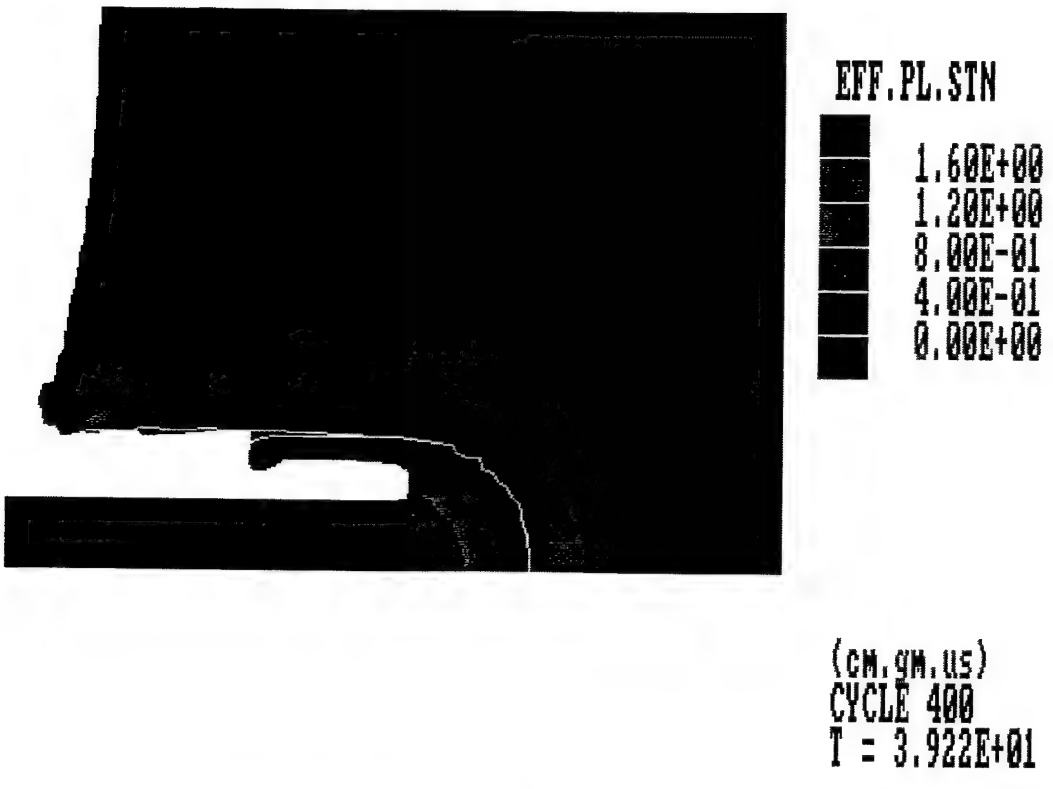

TUNGSTEN INTO STEEL

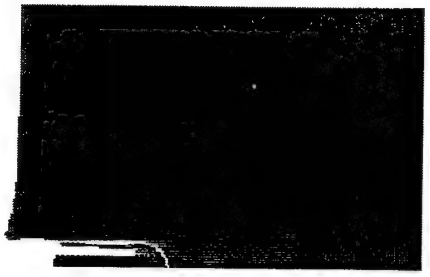

MATERIAL
STATUS

HYDRO
ELASTIC
PLASTIC
FAILED

(cm,gm,us)
CYCLE 800
T = 7.949E+01

TUNGSTEN INTO STEEL

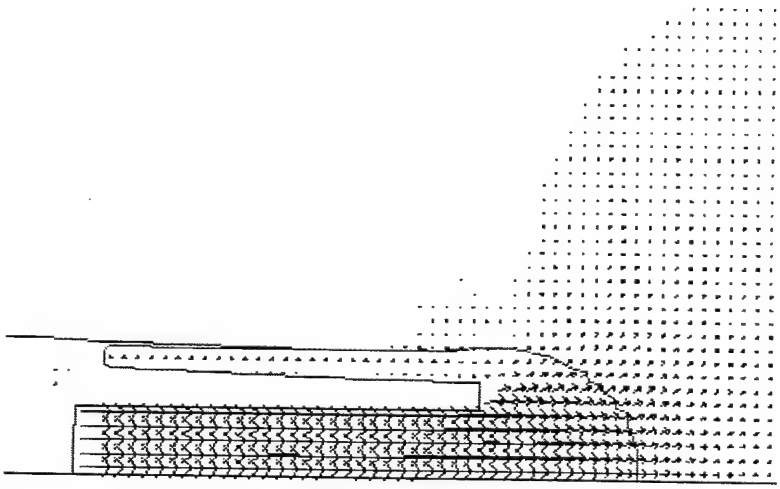

VELOCITY
VECTORS

Scale

8.000E-01

Maximum
Velocity
1.460E-01

Scale
1.300E+00
(cm,gm,us)
CYCLE 800
T = 7.949E+01

TUNGSTEN INTO STEEL

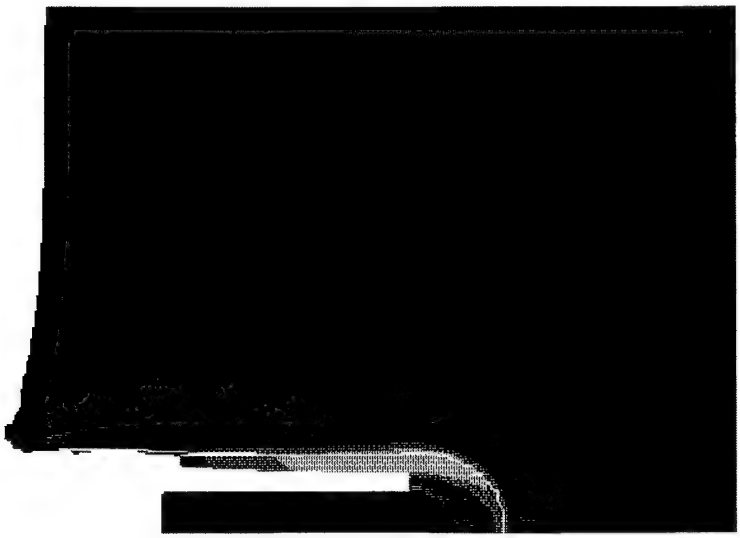

(cm.gm.us)
CYCLE 800
T = 7.949E+01

TUNGSTEN INTO STEEL

(cm.gm.us)
CYCLE 1200
T = 1.219E+02

TUNGSTEN INTO STEEL

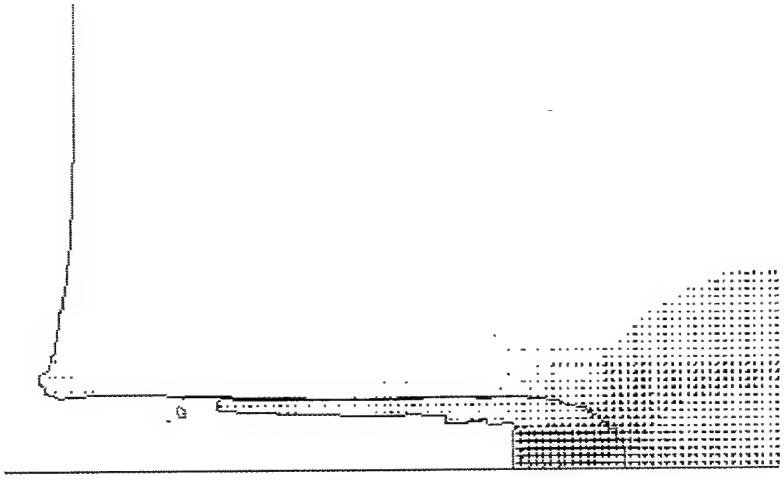

VELOCITY
VECTORS

Scale

8.000E-01

Maximum
Velocity
1.460E-01

Scale

2.400E+00
(cm.gm.us)
CYCLE 1200
T = 1.219E+02

TUNGSTEN INTO STEEL

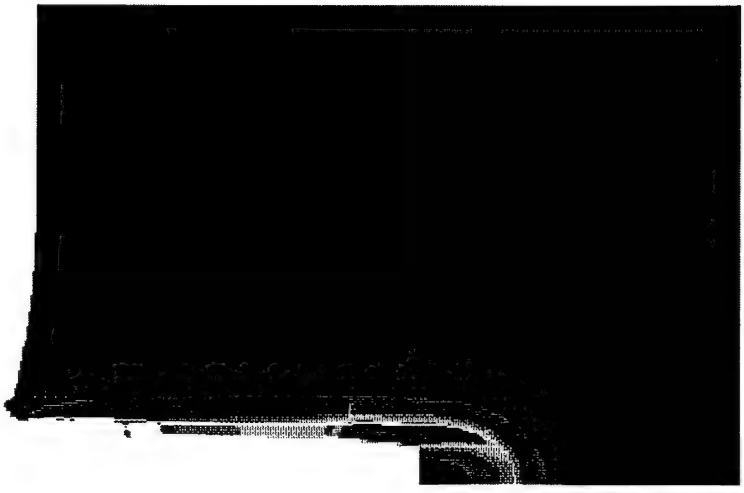

EFF.PL.STN

2.80E+00
2.40E+00
2.00E+00
1.60E+00
1.20E+00
8.00E-01
4.00E-01
0.00E+00

(cm.gm.us)
CYCLE 1200
T = 1.219E+02

TUNGSTEN INTO STEEL

Appendix A5

$\beta = 0.25$

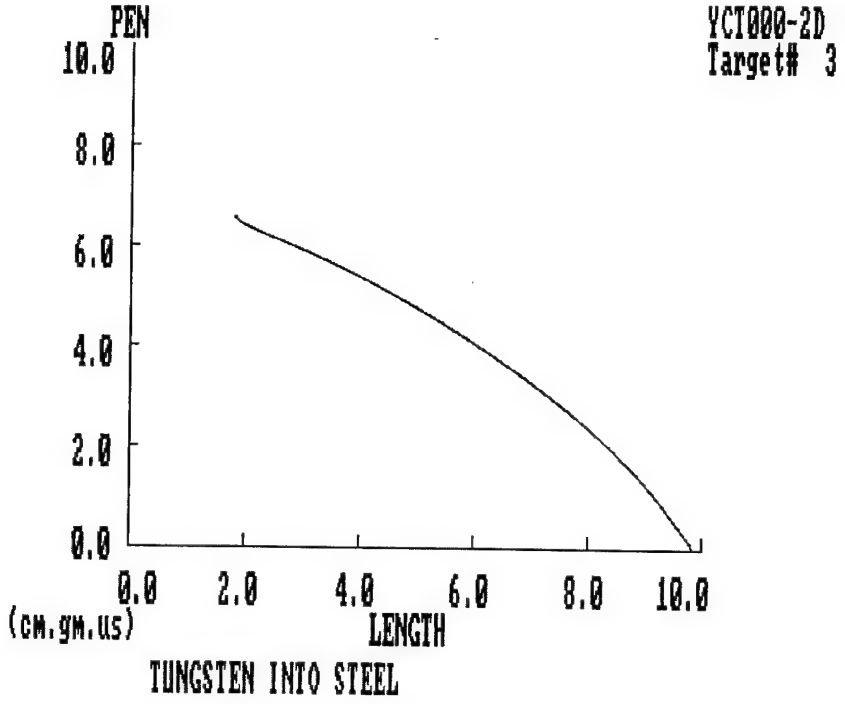
PEN
YCT000-2D
Target# 3
10.0
8.0
6.0
4.0
2.0
0.0
0.0
2.0
4.0
6.0
8.0
10.0
(cm.gm.us)
LENGTH
TUNGSTEN INTO STEEL

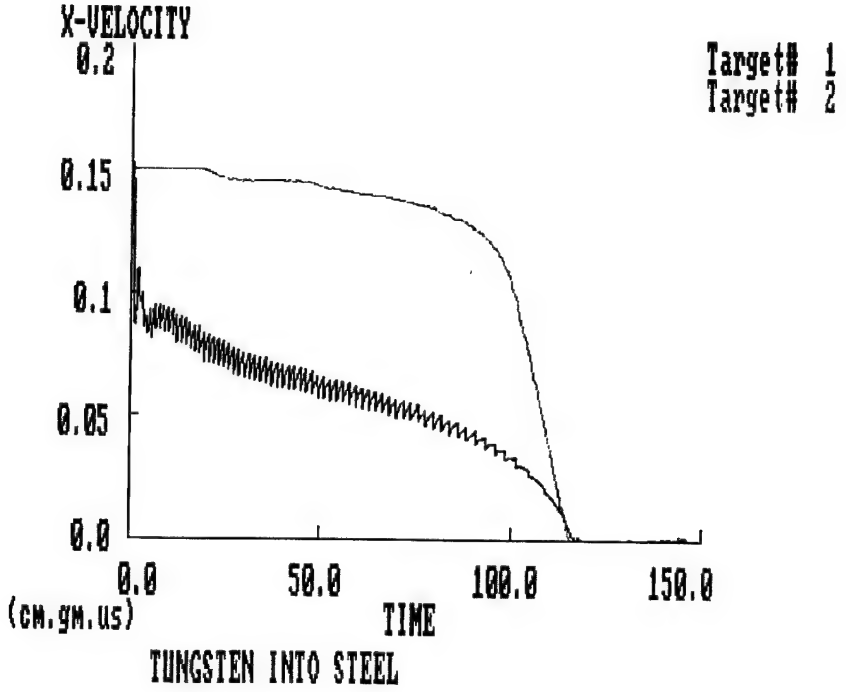
X-VELOCITY
Target# 1
Target# 2
0.2
0.15
0.1
0.05
0.0
0.0
50.0
100.0
150.0
(cm.gm.us)
TIME
TUNGSTEN INTO STEEL

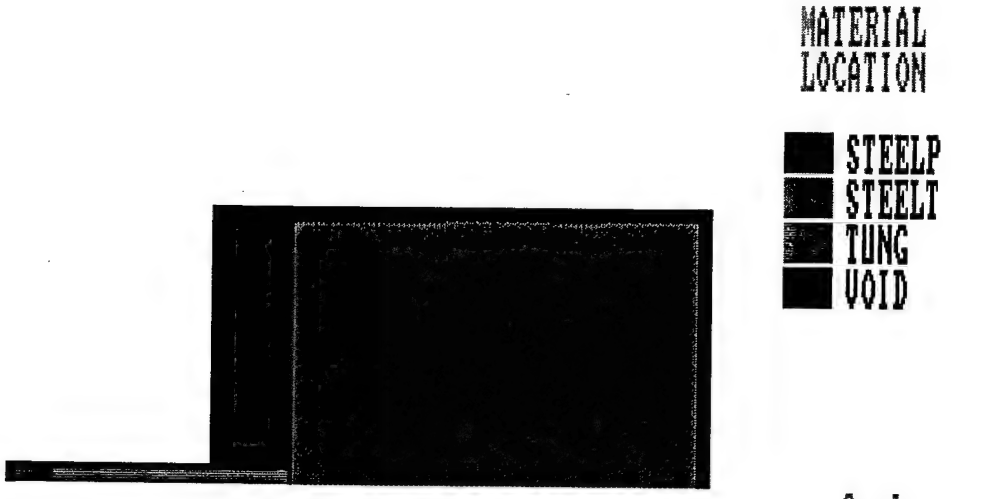

TUNGSTEN INTO STEEL

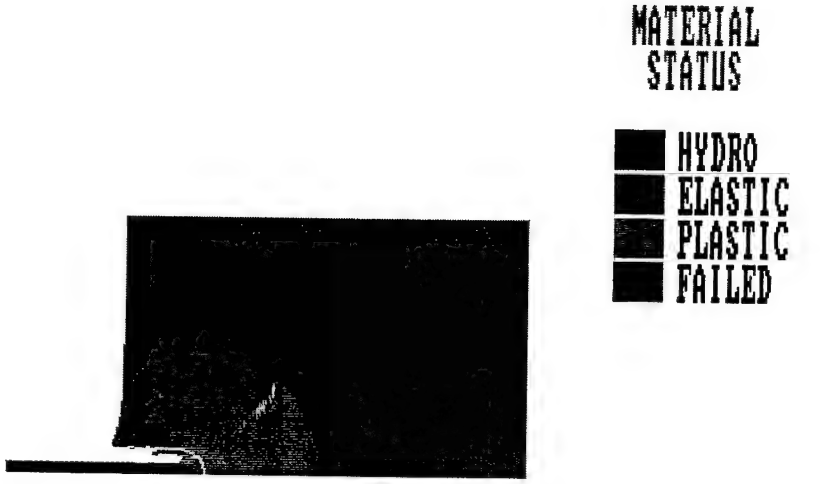

TUNGSTEN INTO STEEL

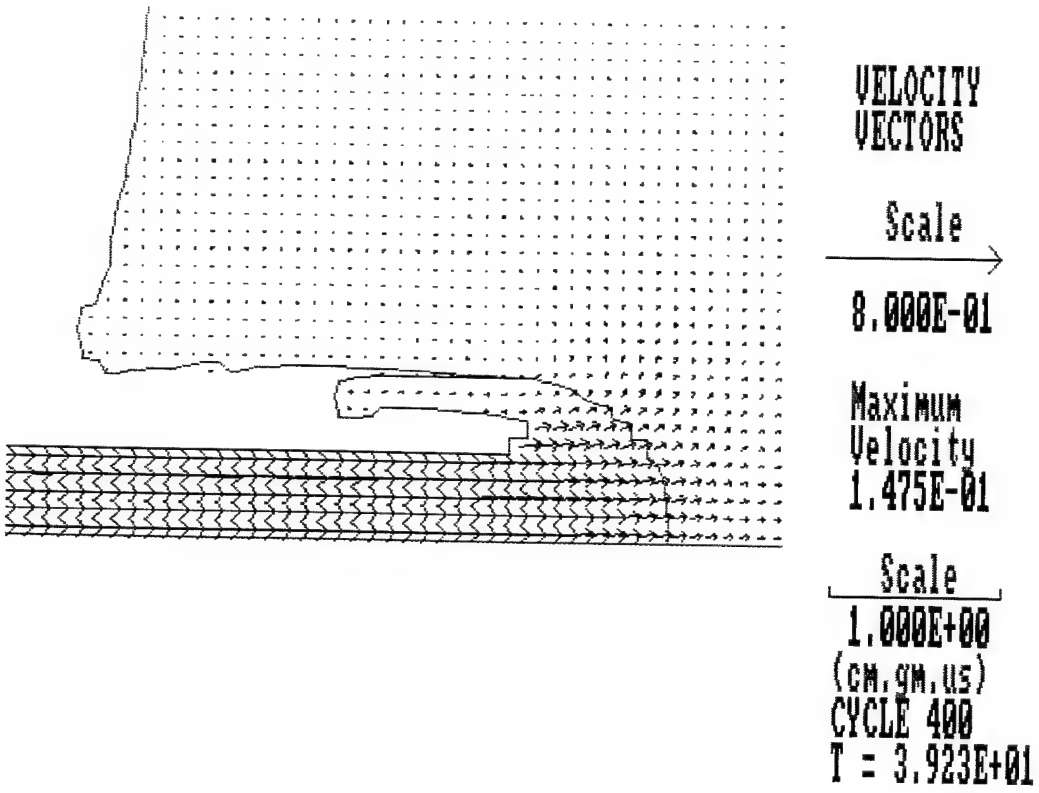

TUNGSTEN INTO STEEL

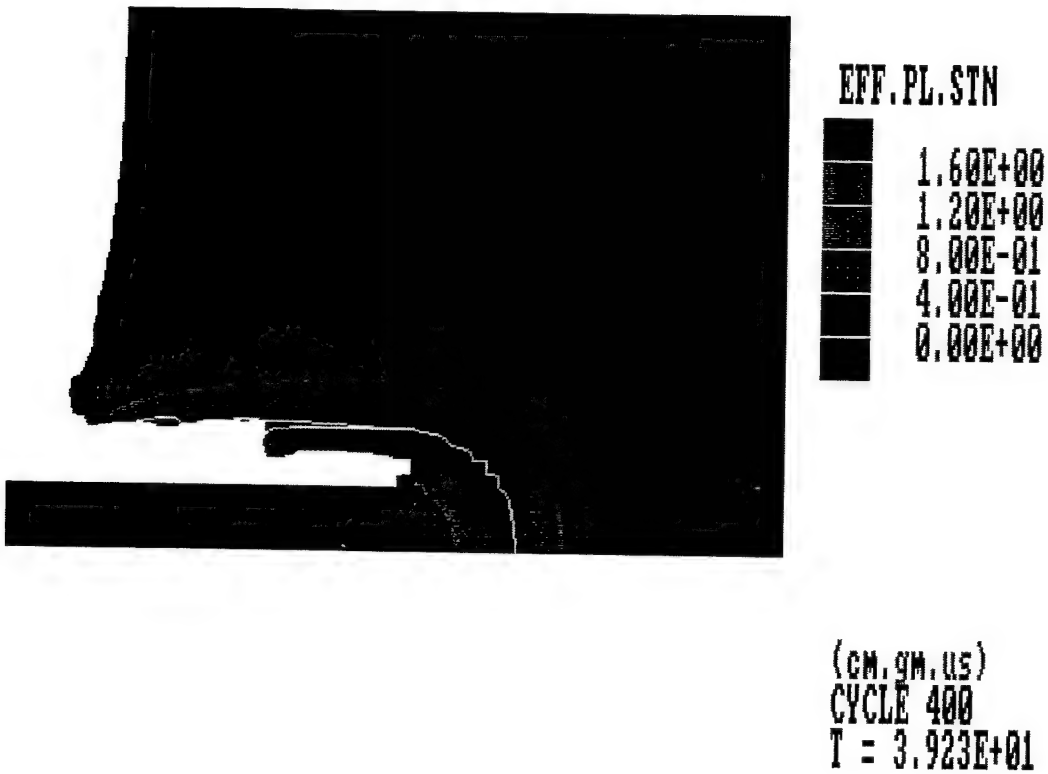

TUNGSTEN INTO STEEL

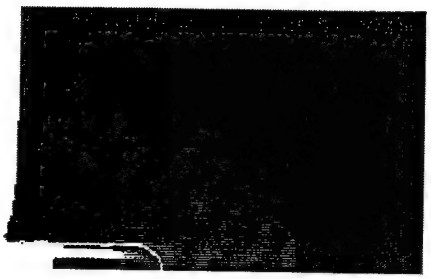

TUNGSTEN INTO STEEL

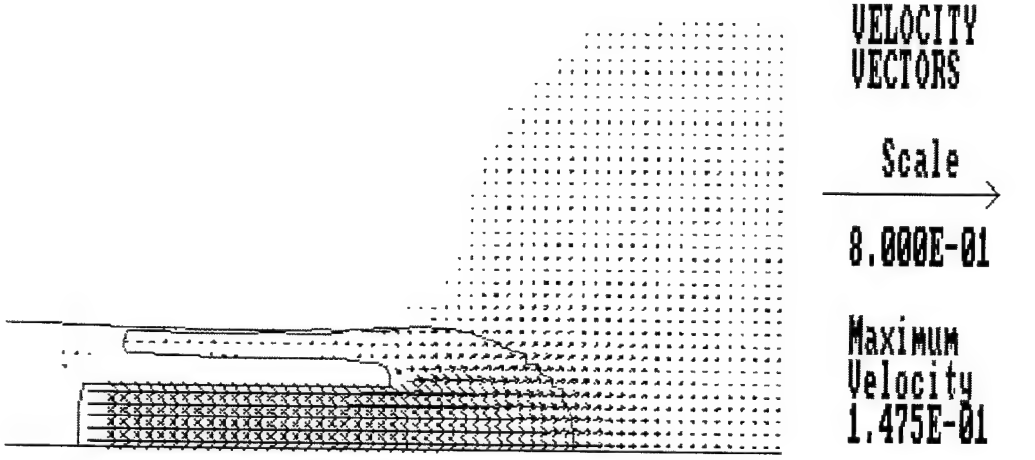

TUNGSTEN INTO STEEL

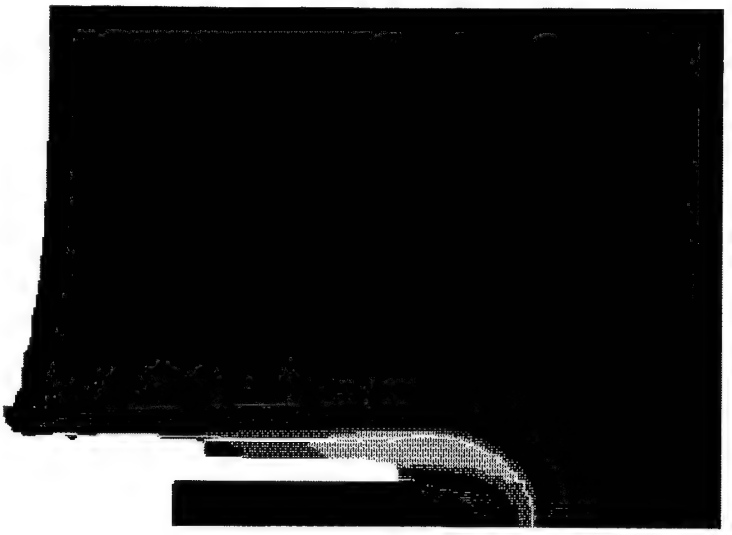

TUNGSTEN INTO STEEL

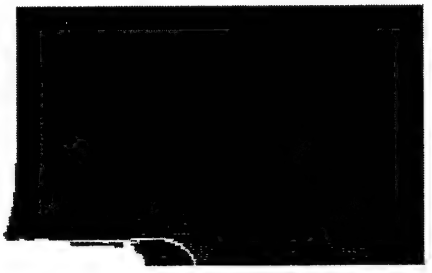

TUNGSTEN INTO STEEL

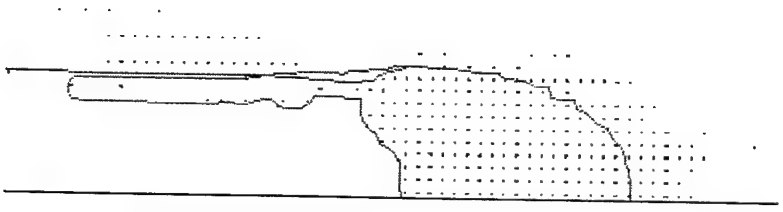

VELOCITY
VECTORS

Scale

8.000E-01

Maximum
Velocity
1.475E-01

Scale
1.400E+00
(cm,gm,us)
CYCLE 1200
T = 1.228E+02

TUNGSTEN INTO STEEL

EFF.PL.STN

2.80E+00
2.40E+00
2.00E+00
1.60E+00
1.20E+00
8.00E-01
4.00E-01
0.00E+00

(cm,gm,us)
CYCLE 1200
T = 1.228E+02

TUNGSTEN INTO STEEL

Appendix A6

$\beta = 0.50$

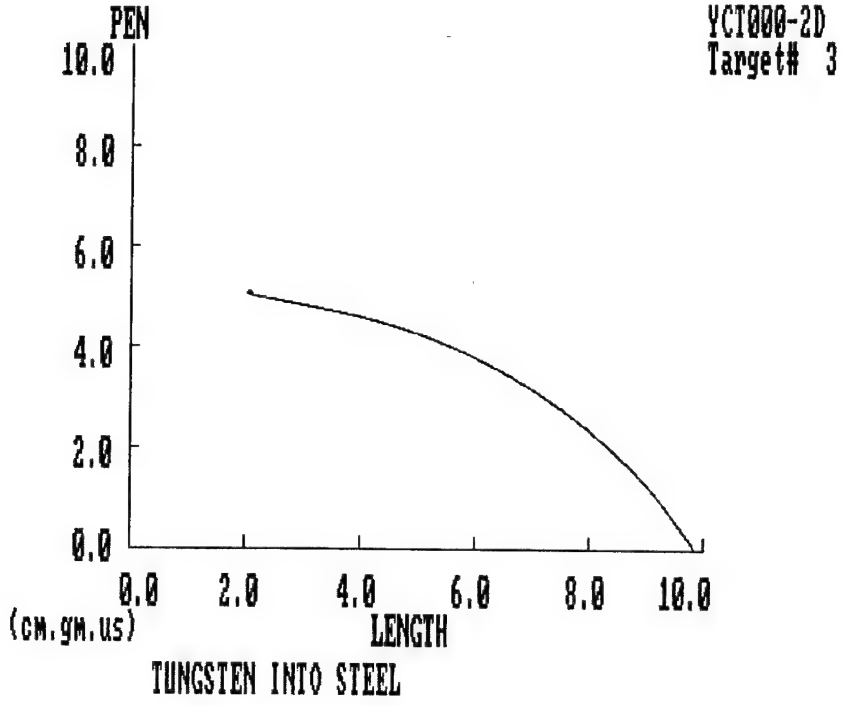
PEN
YCT000-2D
Target# 3
10.0
8.0
6.0
4.0
2.0
0.0
0.0
2.0
4.0
6.0
8.0
10.0
(cm.gm.us)
LENGTH
TUNGSTEN INTO STEEL

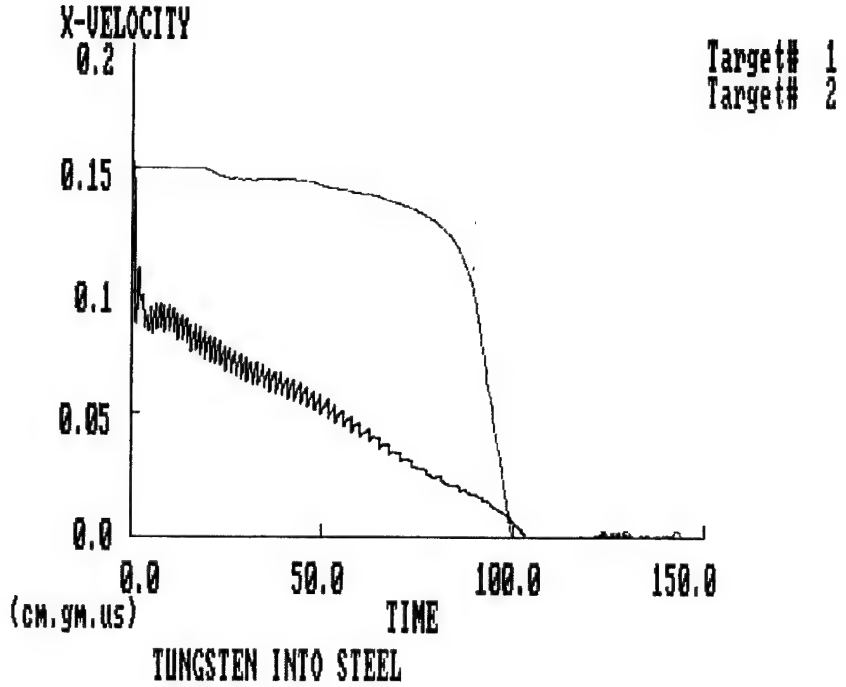
X-VELOCITY
Target# 1
Target# 2
0.2
0.15
0.1
0.05
0.0
0.0
50.0
100.0
150.0
(cm.gm.us)
TIME
TUNGSTEN INTO STEEL

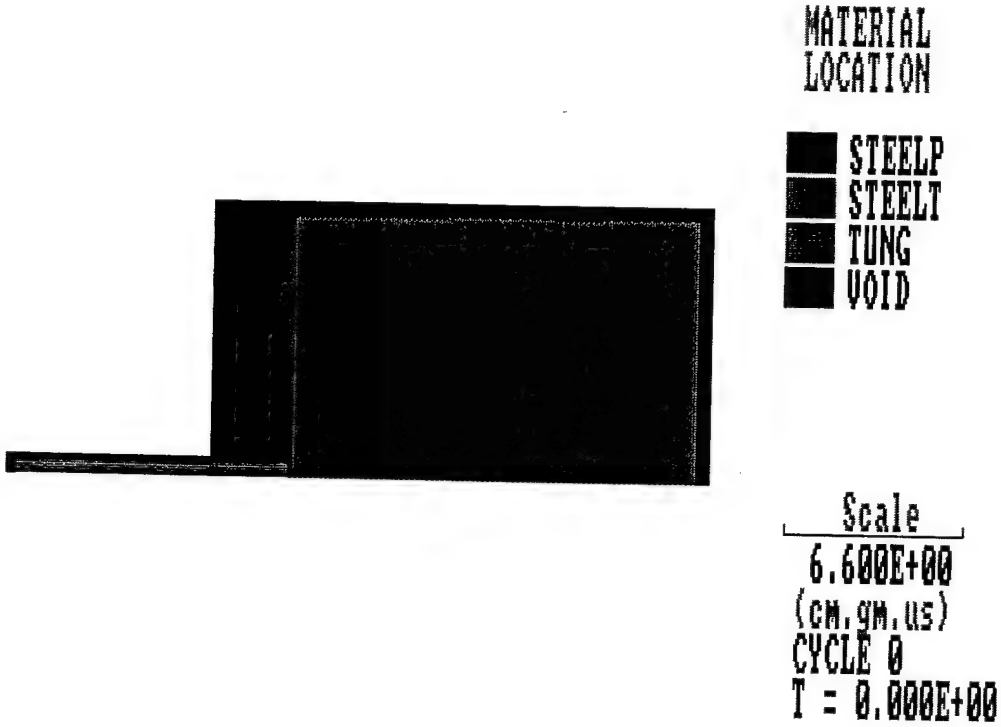

TUNGSTEN INTO STEEL

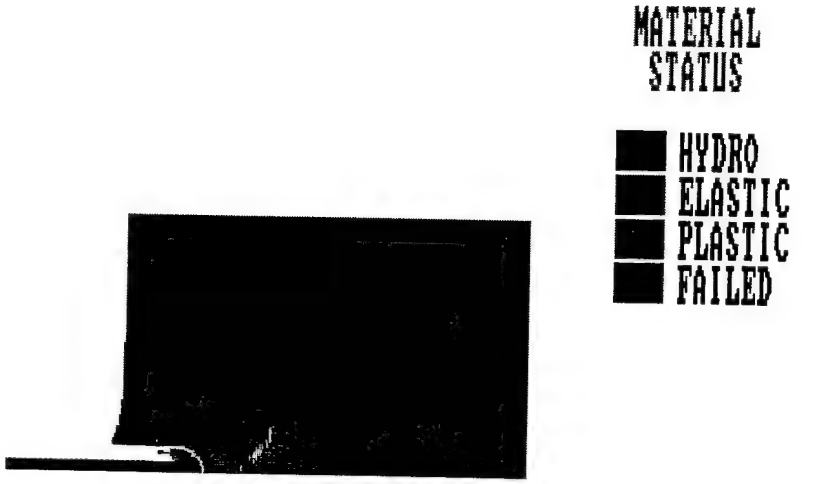

TUNGSTEN INTO STEEL

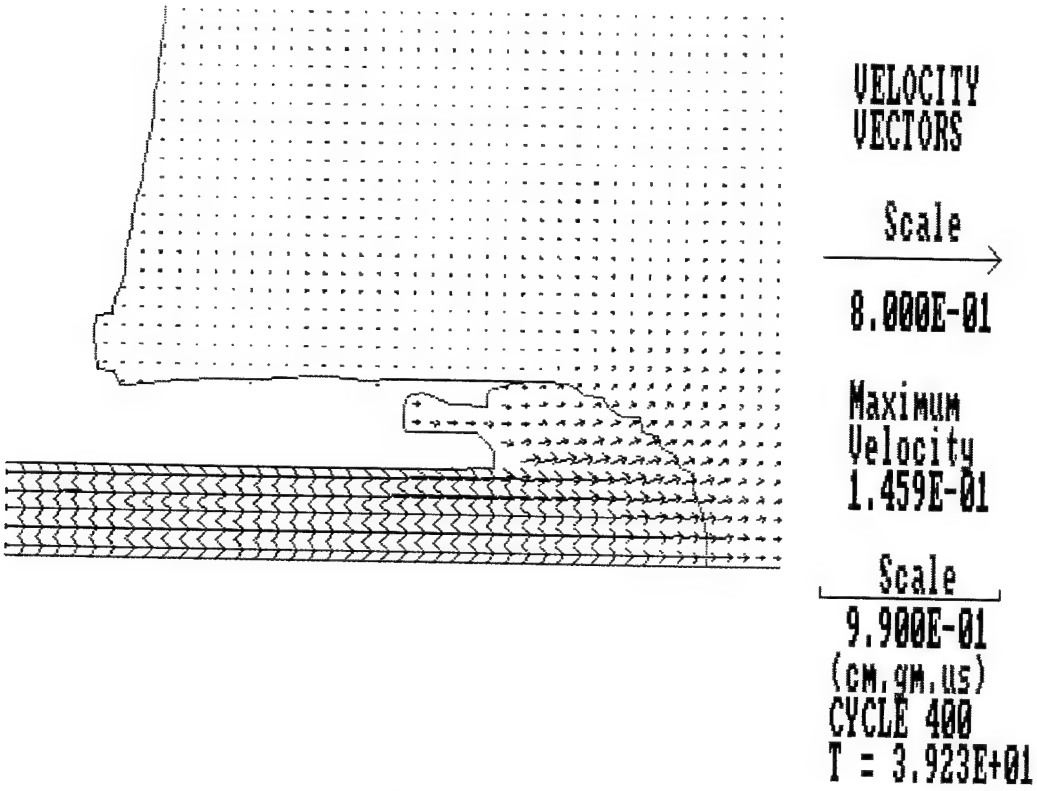

TUNGSTEN INTO STEEL

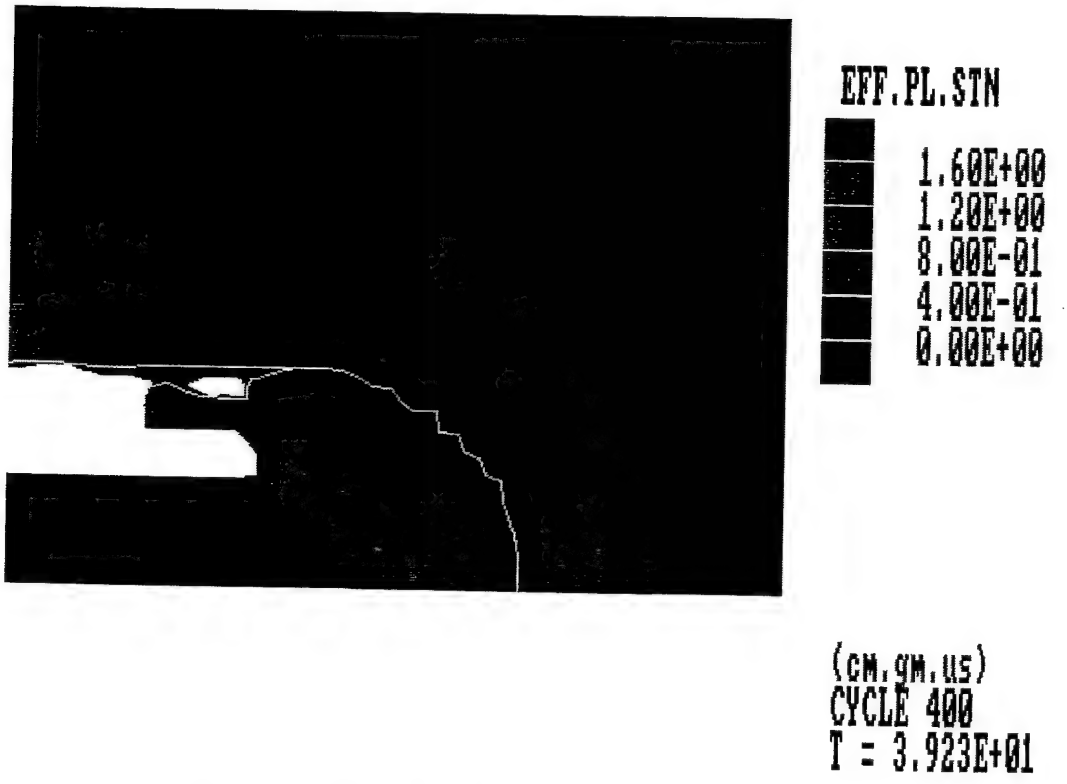

TUNGSTEN INTO STEEL

TUNGSTEN INTO STEEL

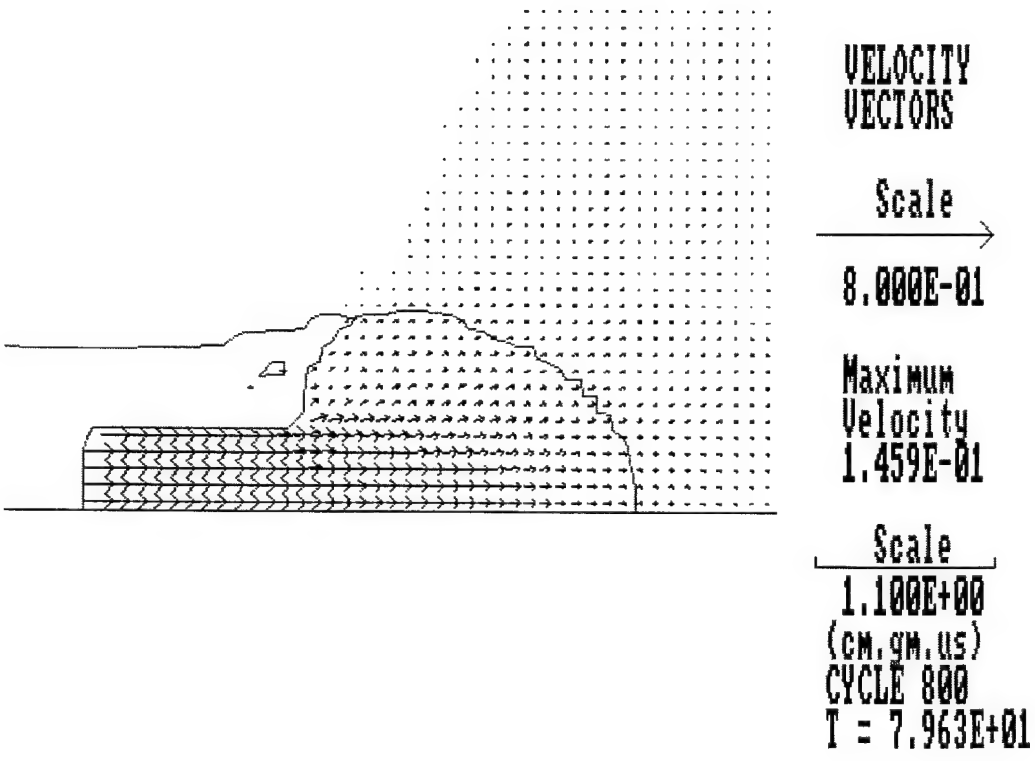

TUNGSTEN INTO STEEL

TUNGSTEN INTO STEEL

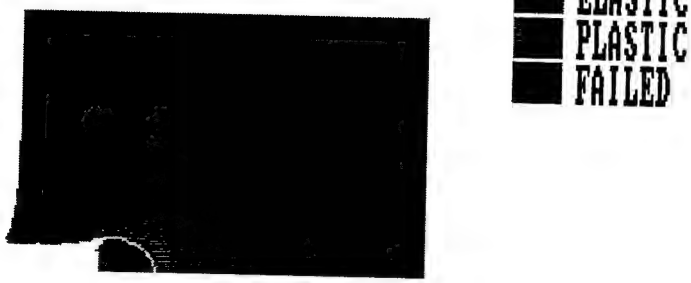

TUNGSTEN INTO STEEL

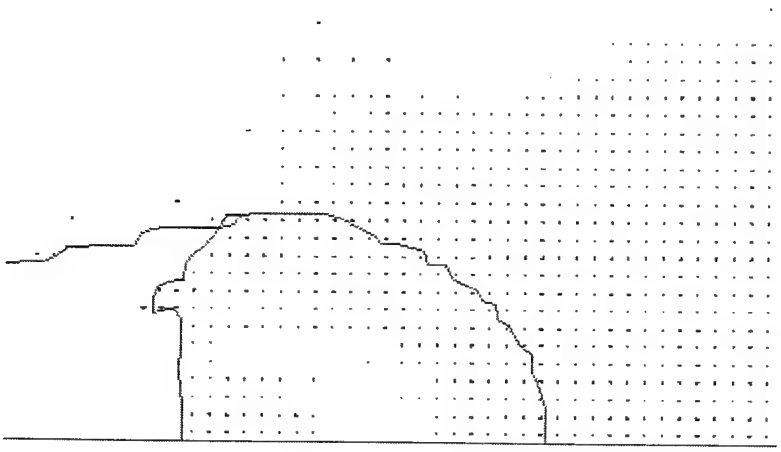

TUNGSTEN INTO STEEL

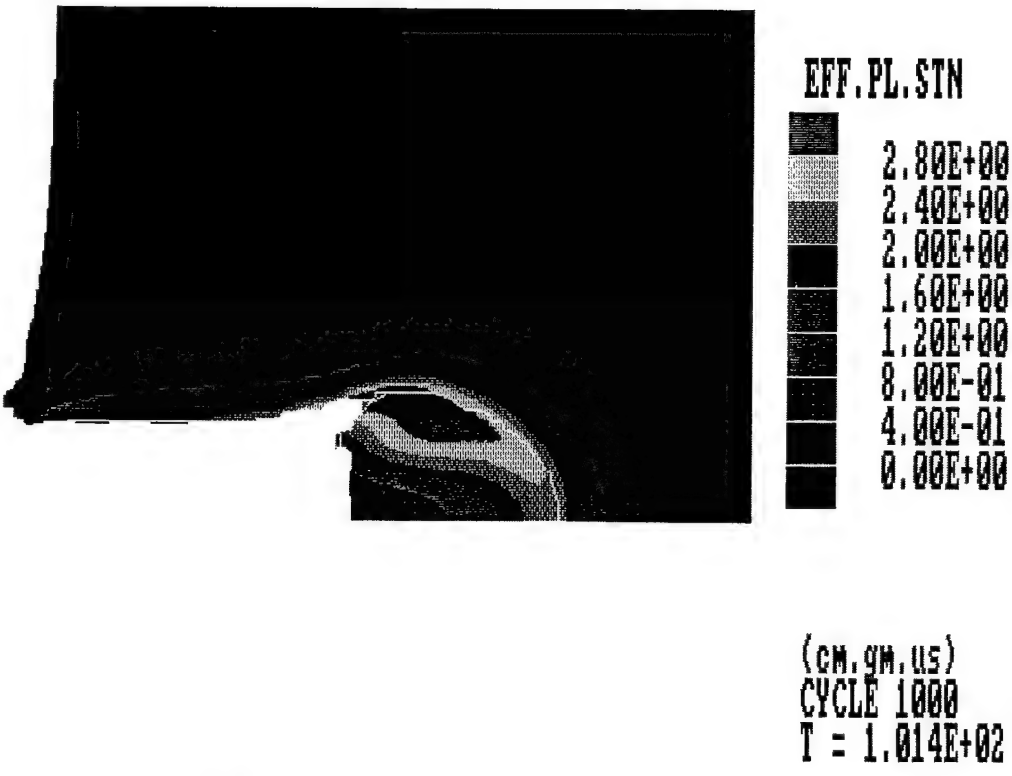

TUNGSTEN INTO STEEL

Appendix A7

$\beta = 1.00$

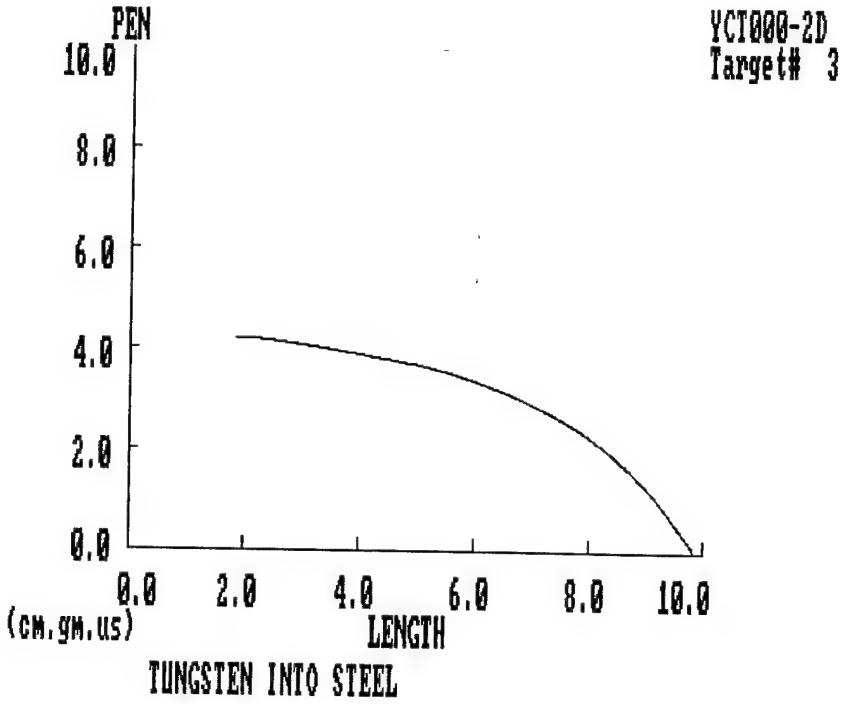
PEN
YCT000-2D
Target# 3
10.0
8.0
6.0
4.0
2.0
0.0
0.0
2.0
4.0
6.0
8.0
10.0
(cm.gm.us)
LENGTH
TUNGSTEN INTO STEEL

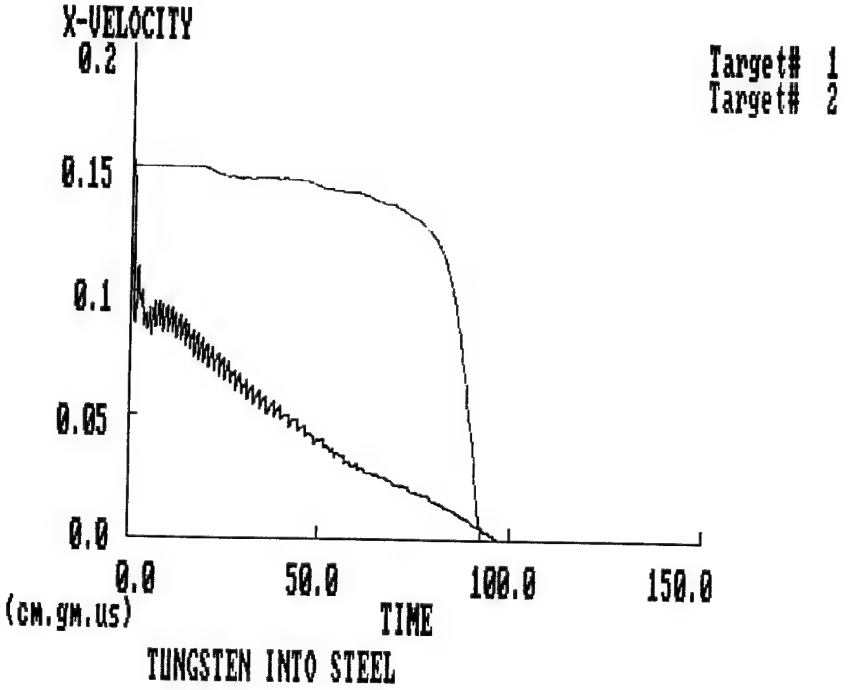
X-VELOCITY
Target# 1
Target# 2
0.2
0.15
0.1
0.05
0.0
0.0
50.0
100.0
150.0
(cm.gm.us)
TIME
TUNGSTEN INTO STEEL

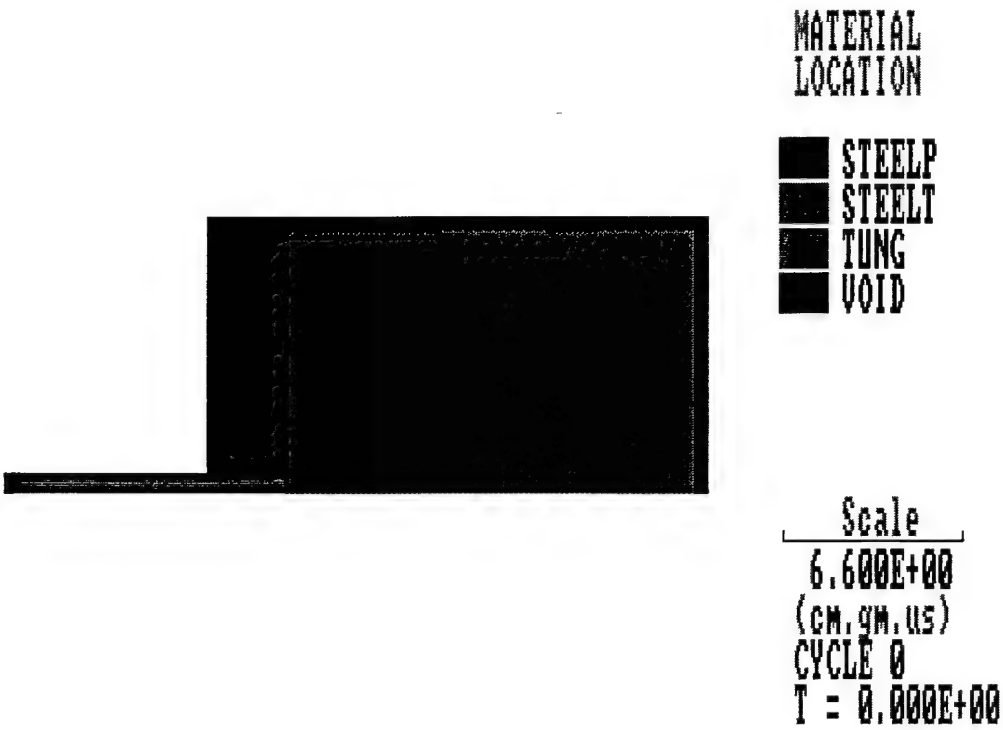

TUNGSTEN INTO STEEL

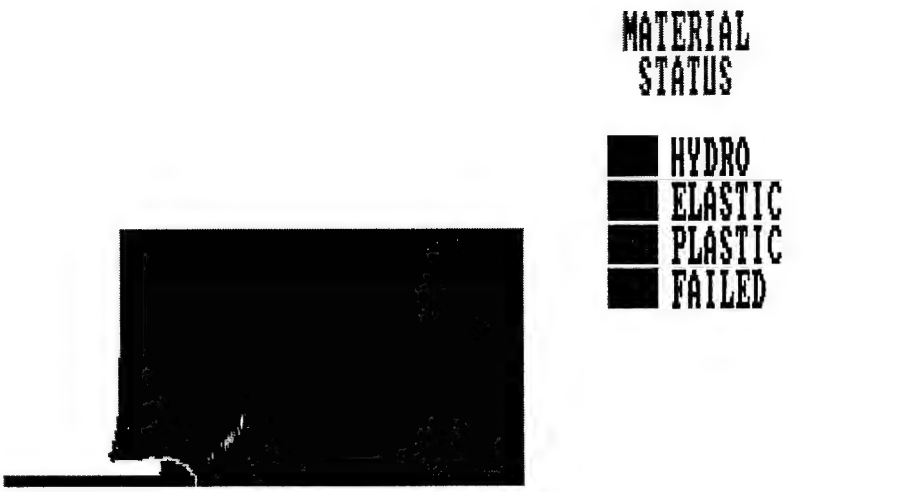

TUNGSTEN INTO STEEL

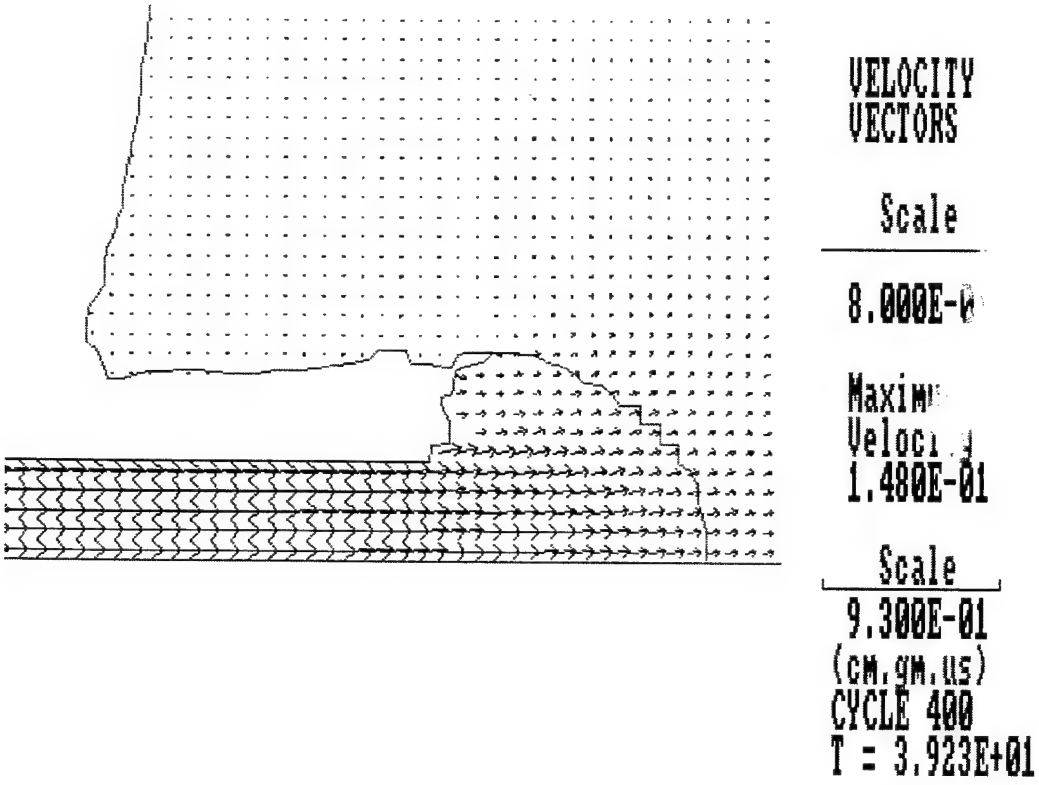

TUNGSTEN INTO STEEL

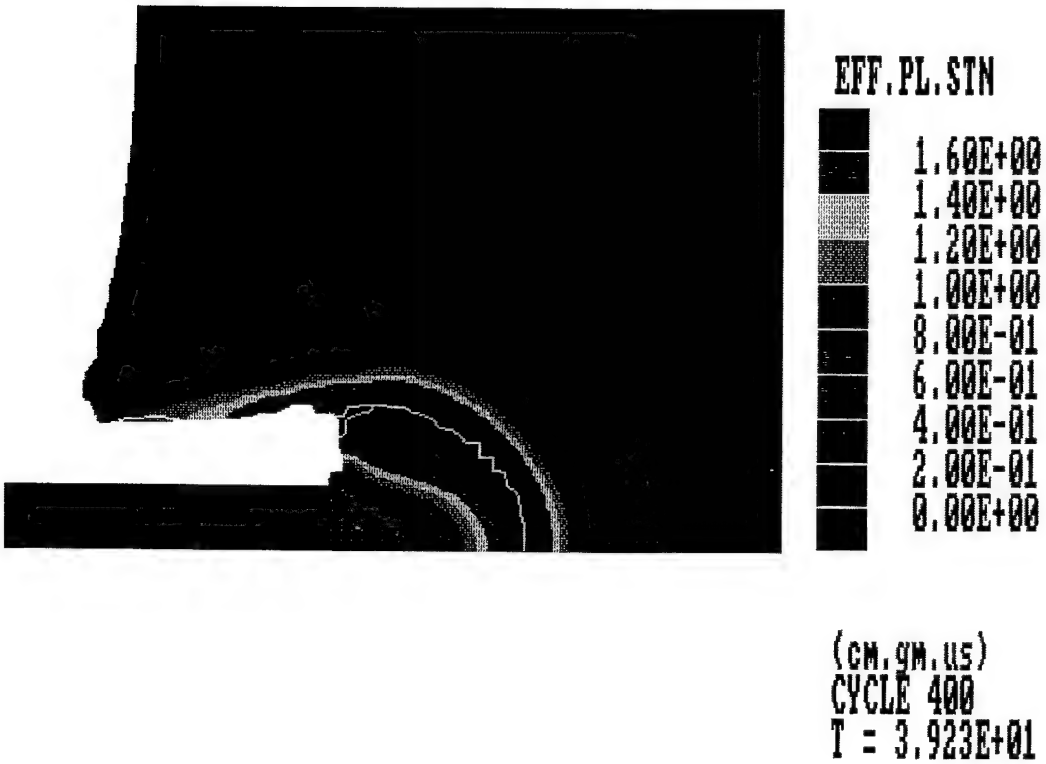

TUNGSTEN INTO STEEL

TUNGSTEN INTO STEEL

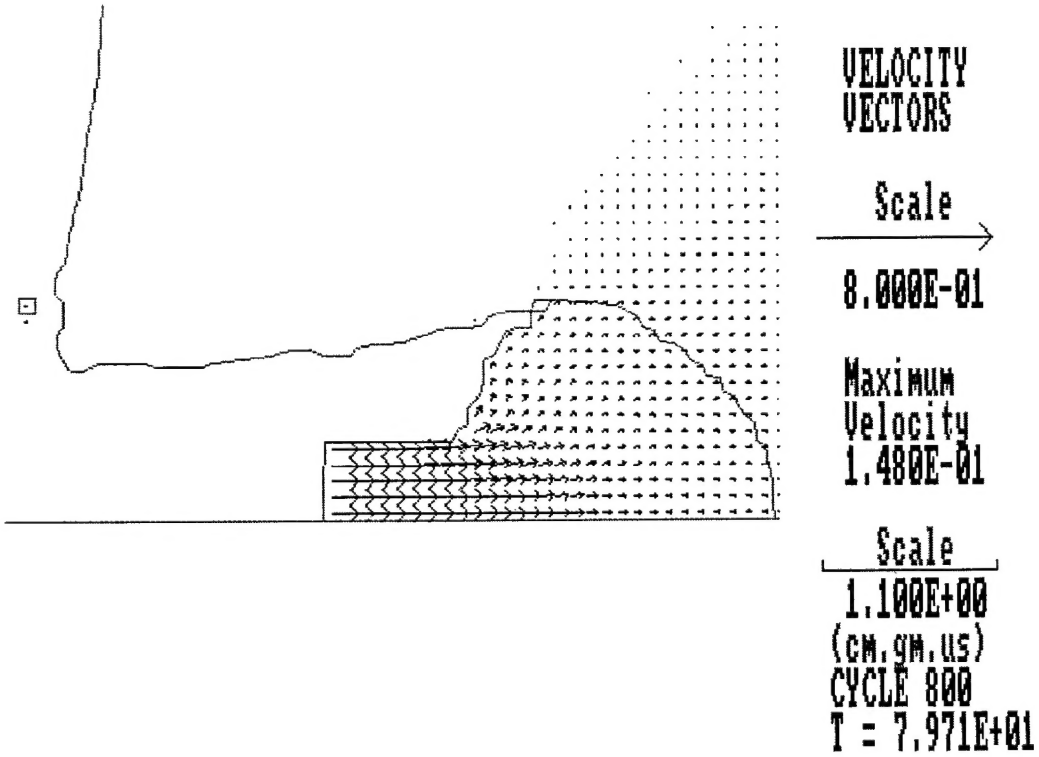

TUNGSTEN INTO STEEL

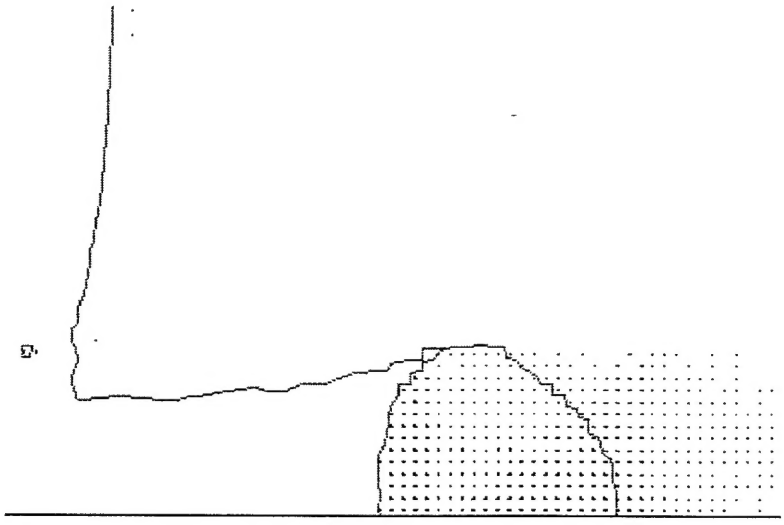

VELOCITY
VECTORS

Scale

8.000E-01

Maximum
Velocity
1.480E-01

Scale
1.500E+00
(cm,gm,us)
CYCLE 1000
T = 1.018E+02

TUNGSTEN INTO STEEL

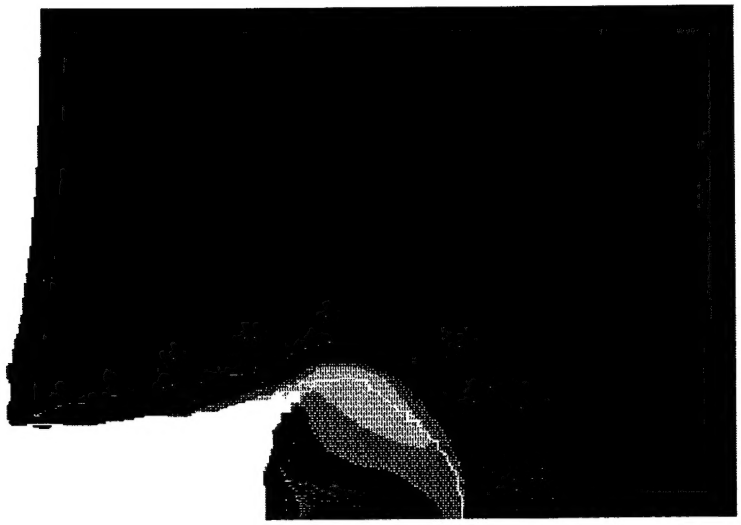

EFF.PL.STN

2.40E+00
2.00E+00
1.60E+00
1.20E+00
8.00E-01
4.00E-01
0.00E+00

(cm,gm,us)
CYCLE 1000
T = 1.018E+02

TUNGSTEN INTO STEEL

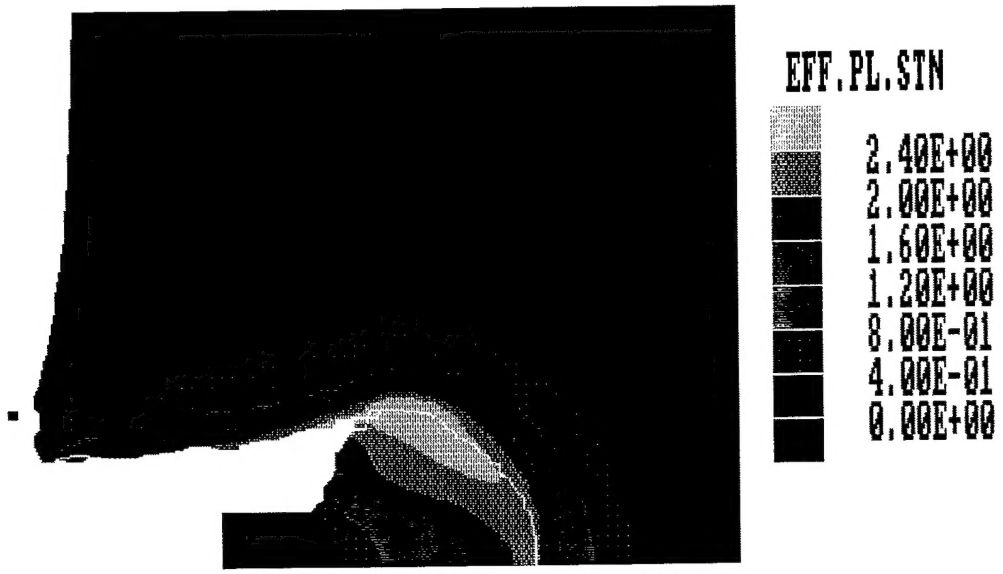

TUNGSTEN INTO STEEL

TUNGSTEN INTO STEEL

Distribution List

Administrator
Defense Technical Information Center
Attn: DTIC-DDA
8725 John J. Kingman Road, Ste 0944
Ft. Belvoir, VA 22060-6218

Director
US Army Research Lab
ATTN: AMSRL OP SD TA
2800 Powder Mill Road
Adelphi, MD 20783-1145

Director
US Army Research Lab
ATTN: AMSRL OP SD TL
2800 Powder Mill Road
Adelphi, MD 20783-1145

Director
US Army Research Lab
ATTN: AMSRL OP SD TP
2800 Powder Mill Road
Adelphi, MD 20783-1145

Director
Army Research Laboratory
AMSRL-CI-LP
Technical Library 305
APG, MD 21005-5066